



**HAL**  
open science

## Stabilization of Metastable Thermoelectric Crystalline Phases by Tuning the Glass Composition in the Cu–As–Te System

Jean-Baptiste Vaney, Julie Carreaud, Andrea Piarristeguy, Cédric Morin, Gaëlle Delaizir, Romain Viennois, Maggy Colas, Julie Cornette, Eric Alleno, Judith Monnier, et al.

► **To cite this version:**

Jean-Baptiste Vaney, Julie Carreaud, Andrea Piarristeguy, Cédric Morin, Gaëlle Delaizir, et al.. Stabilization of Metastable Thermoelectric Crystalline Phases by Tuning the Glass Composition in the Cu–As–Te System. *Inorganic Chemistry*, 2017, 57 (2), pp.754 - 767. 10.1021/acs.inorgchem.7b02683 . hal-01685952

**HAL Id: hal-01685952**

**<https://hal.science/hal-01685952>**

Submitted on 19 Feb 2023

**HAL** is a multi-disciplinary open access archive for the deposit and dissemination of scientific research documents, whether they are published or not. The documents may come from teaching and research institutions in France or abroad, or from public or private research centers.

L'archive ouverte pluridisciplinaire **HAL**, est destinée au dépôt et à la diffusion de documents scientifiques de niveau recherche, publiés ou non, émanant des établissements d'enseignement et de recherche français ou étrangers, des laboratoires publics ou privés.

# **Stabilization of new metastable thermoelectric crystalline phases by tuning the glass composition in the Cu-As-Te system**

J. B. Vaney<sup>1,2</sup>, J. Carreaud<sup>3</sup>, A. Piarristeguy<sup>2</sup>, C. Morin<sup>4</sup>, G. Delaizir<sup>3\*</sup>, R. Viennois<sup>2</sup>, M. Colas<sup>3</sup>, J. Cornette<sup>3</sup>, E. Alleno<sup>4</sup>, J. Monnier<sup>4</sup>, M. Bigot<sup>2</sup>, A. P. Gonçalves<sup>5</sup>, E. B. Lopes<sup>5</sup>, G. J. Cuello<sup>6</sup>, V. Nassif<sup>7,8</sup>, C. Candolfi<sup>1</sup>, B. Lenoir<sup>1</sup>, A. Pradel<sup>2</sup>

<sup>1</sup>*Institut Jean Lamour (IJL), UMR 7198 CNRS-Université de Lorraine, 2 allée André Guinier-Campus ARTEM, BP 50840, 54011 Nancy Cedex, France*

<sup>2</sup>*Institut Charles Gerhardt (ICG), UMR 5253 CNRS-Université de Montpellier, France*

<sup>3</sup>*Science des Procédés Céramiques et de Traitements de Surface (SPCTS), UMR CNRS 7315, Centre Européen de la Céramique, Limoges, France*

<sup>4</sup>*Institut de Chimie et des Matériaux de Paris Est (ICMPE), UMR 7182 CNRS, CMTR, Thiais, France*

<sup>5</sup>*C2TN, Instituto Superior Técnico, Universidade de Lisboa, Bobadela, Portugal*

<sup>6</sup>*Institut Laue Langevin, Grenoble, France*

<sup>7</sup>*Université Grenoble Alpes, Grenoble, France*

<sup>8</sup>*CNRS, Institut Néel, Grenoble, France*

## **Abstract**

Recrystallization of amorphous compounds can lead to the stabilization of metastable crystalline phases, which offers an interesting way to unveil novel binary or ternary compounds and control the transport properties of obtained glass-ceramics. Here, we report on a systematic study of the Cu-As-Te glassy system and show that under specific synthesis conditions using the spark plasma sintering technique, the  $\alpha$ -As<sub>2</sub>Te<sub>3</sub> and  $\beta$ -As<sub>2</sub>Te<sub>3</sub> binary phases or the previously unreported AsTe<sub>3</sub> phase can be selectively crystallized within an amorphous matrix. The microstructure and transport properties of three different glass-ceramics, each of them containing one of these phases with roughly the same crystalline fraction (~ 30% in volume),

were investigated in detail by means of X-ray diffraction, scanning electron microscopy, neutron thermodiffraction, Raman scattering (experimental and lattice dynamics calculations) and transport properties measurements. The physical properties of the glass-ceramics are compared to both the parent glasses and the pure crystalline phases that could be successfully synthesized. SEM images coupled with Raman spectroscopy evidence a “coast-to-island” or dendritic-like microstructure with micro-sized crystallites. The presence of the crystallized phase results in a significant decrease in the electrical resistivity while maintaining the thermal conductivity to low values. This study demonstrates that new compounds with interesting transport properties can be obtained by recrystallization which in turn, provide a tuning parameter of the transport properties of the parent glasses.

## 1. Introduction

Due to their large optical window extending in the infrared range, chalcogenide glasses can be used as optics for thermal cameras as well as biosensors for medical applications.<sup>1-3</sup> Their low melting temperature ( $< 300\text{ }^{\circ}\text{C}$ ) combined with the ability to easily switching between amorphous and crystalline states make chalcogenide glasses candidates of choice for phase change memories.<sup>4,5</sup> Among their remarkable properties, their high linear and non-linear refractive indices enable applications in the photonic domain.<sup>6</sup> Further, chalcogenide glasses have attracted significant attention in the field of energy as electrolyte for solid-state batteries. In this last application, the crystallization of a Li-based metastable phase ranks glass-ceramic systems among the most competing materials for such applications.<sup>7-9</sup> Similarly, chalcogenide glasses and glass-ceramics have recently driven interest as possible thermoelectric materials due to their high thermopower ( $\alpha > 500\text{ }\mu\text{V K}^{-1}$ ) and extremely low thermal conductivity ( $\lambda < 0.3\text{ W m}^{-1}\text{ K}^{-1}$ ), both properties being two prominent criteria to achieve high thermoelectric

performances, evaluated by the dimensionless thermoelectric figure of merit  $ZT = \alpha^2 T / \rho \lambda$ , where  $T$  is the absolute temperature and  $\rho$  is the electrical resistivity.<sup>10-15</sup>

The main drawback of these materials remains their high electrical resistivity that presently still prevents them from being competitive with state-of-the-art thermoelectric materials such as  $\text{Bi}_2\text{Te}_3$  or  $\text{PbTe}$ .<sup>16-19</sup> However, the partial crystallization of the parent glass in the Cu-As-Te ternary system has proved to be an efficient pathway towards reducing the electrical resistivity by several orders of magnitude.<sup>15</sup> This glassy system exhibits a wide vitreous domain leading to a large choice of glass compositions that allows for a fine tuning of its transport properties.

Here, we report on a systematic investigation of the first crystallization of glasses in the Cu-As-Te system. Interestingly, we show that specific binary phases can be selectively crystallized within the glassy matrix upon heating by controlling the initial glass composition. Some of these crystalline compounds are metastable and can only be stabilized through this peculiar soft devitrification process, making this technique a powerful tool to produce such phases. Three compositions in the Cu-As-Te vitreous domain have been carefully chosen to achieve the stabilization of three different crystalline phases, namely  $\alpha\text{-As}_2\text{Te}_3$ , the metastable binary  $\beta\text{-As}_2\text{Te}_3$  and the as-yet unknown binary  $\text{AsTe}_3$ . The influence of the nature of the crystalline phase on the microstructure and physical properties of the glass-ceramics has been investigated in details by means of powder X-ray diffraction, neutron thermodiffraction, Raman scattering and transport properties measurements. These experimental results are complemented by lattice dynamics calculations. Finally, the physical properties of these glass-ceramics are compared to both the parent glass and the pure crystalline phases that have been successfully synthesized.

## 2. Experimental

### 2.1 Synthesis

Three glassy samples of nominal compositions,  $\text{Cu}_{20}\text{As}_{35}\text{Te}_{45}$ ,  $\text{Cu}_{15}\text{As}_{30}\text{Te}_{55}$  and  $\text{Cu}_{15}\text{As}_{20}\text{Te}_{65}$  were synthesized in silica tubes sealed under secondary vacuum. Starting elements, As (Goodfellow, 99.99%), Te (5N+, 99.99%) and Cu (Sigma-Aldrich, 99.999%) were first weighed in stoichiometric quantities (for a total batch of  $\sim 4\text{g}$ ) and introduced in a silica tube. The tube was subsequently evacuated, sealed and heated in a furnace with a low heating rate of  $9\text{ K}\cdot\text{h}^{-1}$  up to 1123 K, held at this temperature for 2 hours and finally quenched in a salt-ice-water mixture. The resulting ingots were hand-ground into micron-sized powders.

Spark Plasma Sintering (SPS) of the powders was realized in 10 mm diameter graphite dies with the Dr. Sinter 825 Syntex apparatus. This technique allows obtaining both amorphous bulk samples and glass-ceramics, depending on the temperature program. The sintering temperature was checked by a thermocouple placed inside the graphite die at about 6 mm from the sample. The SPS experimental parameters for the different samples (temperature, dwell time and pressure) will be described in details in section 3.1.

Crystalline  $\alpha\text{-As}_2\text{Te}_3$ ,  $\beta\text{-As}_2\text{Te}_3$  and  $\text{AsTe}_3$  were successfully synthesized in polycrystalline form.  $\beta\text{-As}_2\text{Te}_3$  was synthesized by the melt-quenching technique (melting at 923 K) and densified by cold pressing.<sup>20</sup>  $\alpha\text{-As}_2\text{Te}_3$  was obtained by annealing the  $\beta\text{-As}_2\text{Te}_3$  phase at 553 K for 72 hours. The resulting ingot was ground into fine powders and densified by SPS at 618 K for 2 minutes under a pressure of 50 MPa.  $\text{AsTe}_3$  was synthesized from the full and congruent crystallization of the parent glass obtained by the twin-roller quenching technique.<sup>21</sup> The fine powder was subsequently densified by SPS at 453 K for 30 minutes under a pressure of 50 MPa.

## 2.2 Structural and chemical characterization

To verify the amorphous nature of the samples and to identify the crystalline phases, powder X-ray diffraction (PXRD) measurements on the surface of the SPS bulk samples were carried out at 300 K using a D8 Bruker diffractometer equipped with a Vantec 1D-detector ( $\lambda_{\text{Cu}}=1.5406 \text{ \AA}$ ).

The density of the bulk samples was determined through the Archimedean principle using a Kern balance. This balance enables weighing solids in air ( $m_{\text{air}}$ ) as well as in a solvent (in our case, water  $m_{\text{water}}$ ). When the density of the buoyancy medium is known ( $\delta_0$ ), the density of the solid ( $\delta$ ) is calculated as follows:

$$\delta = \frac{m_{\text{air}}}{m_{\text{air}} - m_{\text{water}}} \delta_0 \quad (1)$$

The microstructure of both the amorphous and glass-ceramic bulk samples synthesized by SPS was investigated on well-polished surface using a Cambridge Scanning Electron Microscope (SEM). Composition of crystalline phases was estimated using Energy Dispersive X-Ray Spectroscopy (EDXS). For the unknown AsTe<sub>3</sub> crystalline phase, the composition was also determined using Electron Probe Micro Analysis (EPMA).

The thermal behavior of the as-quenched samples was studied by Differential Scanning Calorimetry (DSC) performed using TA instrument AQ100 equipment from 300 up to 573 K using a heating rate of 10 K.min<sup>-1</sup>.

## 2.3 Neutron thermodiffraction

Neutron thermodiffraction experiments were carried out to probe the crystallization process undergone by the glasses upon heating. These measurements were performed using the D1B instrument at the Institut Laue–Langevin (ILL) in Grenoble (France) with a nominal

wavelength of 2.52 Å. The three glassy samples ( $\text{Cu}_{20}\text{As}_{35}\text{Te}_{45}$ ,  $\text{Cu}_{15}\text{As}_{30}\text{Te}_{55}$  and  $\text{Cu}_{15}\text{As}_{20}\text{Te}_{65}$ ) were placed under vacuum inside unsealed cylindrical vanadium containers (inner diameter of 10 mm). Using a dedicated D1B furnace (vertical top loading furnace), neutron diffraction spectra were continuously collected on the samples subjected to the following heating ramps: from 300 to 363 K at a rate of 5 K.min<sup>-1</sup> and from 363 to 473 K at a lower rate of 0.1 K.min<sup>-1</sup>. For the cooling process, the furnace was simply switched off to allow the samples to reach room temperature in ‘free fall’. Rietveld refinements were performed on the neutron patterns measured at high temperature on the three fully crystallized Cu-As-Te glasses, with the help of the program Fullprof.<sup>22</sup> Prior to these refinements, the crystalline phase identification was carried out with the commercial software EVA (Bruker), after conversion of the ILL data file to the proper format. The nuclear scattering lengths published by Sears were used.<sup>23</sup> The neutron wavelength of the ILL-D1B two-circle diffractometer  $\lambda = 2.522$  Å was calibrated with the help of a TiO<sub>2</sub> standard and the Gaussian broadening of the lines by the instrument was modelled by a Cagliotti function with its parameters fixed to the values  $U = 1.4066$ ,  $V = -0.2154$  and  $W = 0.0890$ . In all three cases, the refined parameters were the phase fractions, the zero-shift, the lattice parameters, the atomic positions and a simple Scherrer size to account for the Lorentzian broadening of the lines by the sample. The thermal displacement parameters were held fixed to  $B = 1.2$ , a value large enough to account for the “natural” disorder that is usually seen in these phases crystallized from a glass.

## 2.4 Raman scattering

Raman spectroscopy characterizations of  $\text{Cu}_{20}\text{As}_{35}\text{Te}_{45}$ ,  $\text{Cu}_{15}\text{As}_{30}\text{Te}_{55}$  and  $\text{Cu}_{15}\text{As}_{20}\text{Te}_{65}$  glass-ceramics and of  $\alpha\text{-As}_2\text{Te}_3$ ,  $\beta\text{-As}_2\text{Te}_3$ ,  $\text{AsTe}_3$  crystalline phases were performed using an In Via Reflex Renishaw Raman spectrophotometer. We used the 2D mapping module in

confocal mode, which gives access to high definition maps and high spatial resolution images due to the large number of recorded spectra. The maps ( $25\mu\text{m} \times 25\mu\text{m}$  with a step of  $1\mu\text{m}$ ) were recorded using a  $\times 50$  objective with  $785\text{ nm}$  wavelength excitation and low power ( $0.03\text{ mW}$ ) to avoid any damage of the sample. The use of a  $1200\text{ grooves/mm}$  grating permitted to reach a resolution of  $2.4\text{ cm}^{-1}$ .

## 2.5 Lattice dynamics calculation details of $\alpha$ - and $\beta$ -As<sub>2</sub>Te<sub>3</sub> pure crystalline phases

The theoretical Raman band positions of  $\alpha$ -As<sub>2</sub>Te<sub>3</sub> and  $\beta$ -As<sub>2</sub>Te<sub>3</sub> pure crystalline phases were modeled using first-principles calculations performed within the Density Functional Theory (DFT) with the plane-wave VASP package and Projector Augmented Wave (PAW) pseudopotentials.<sup>24,25</sup> Because the crystal structure of AsTe<sub>3</sub> is so far unresolved, the investigation was restricted to  $\alpha$ - and  $\beta$ - As<sub>2</sub>Te<sub>3</sub>. Two types of exchange-correlation functionals were used: the standard Generalized Gradient Approximation (GGA) functional of Perdew, Burke and Erzenhof (PBE) type and the corrected van der Waals functional of PBE-D2 type from Grimme that includes empirically damped atom-pairwise dispersion corrections of the form  $C_6R^{-6}$ .<sup>26,27</sup> In all calculations, an energy cut-off of  $500\text{ eV}$  was used. The  $k$ -mesh used was  $15 \times 15 \times 15$  and  $12 \times 12 \times 12$  for the rhombohedral  $\beta$ -As<sub>2</sub>Te<sub>3</sub> and monoclinic  $\alpha$ -As<sub>2</sub>Te<sub>3</sub> phases, respectively. The structures and atomic positions were relaxed until the residual forces were smaller than  $10^{-4}$  and  $10^{-5}\text{ eV}\cdot\text{\AA}^{-1}$ , respectively. Phonon calculations were performed at the  $\Gamma$  point of the Brillouin zone using the Density Functional Perturbation Theory (DFPT) as implemented in the VASP code and the atoms were displaced by  $0.015\text{ \AA}$  from their equilibrium positions.<sup>28</sup> With these conditions, the calculations were highly converged.

## 2.6 Transport properties measurements

Electrical resistivity and thermopower measurements were carried out simultaneously with a ZEM-3 (ULVAC-RIKO) system between 300 and 375 K. Bar-shaped samples of typical dimensions  $1 \times 1.5 \times 8 \text{ mm}^3$  were cut with a diamond wire-saw. Uncertainty for electrical resistivity and thermopower was  $\pm 6\%$  and  $\pm 5\%$ , respectively. The thermal conductivity was determined via thermal diffusivity measurements carried out with a LFA 427 (Netzsch) equipment. Cylinder-shaped samples were used for these experiments that were performed under argon atmosphere between 300 and 375 K. The uncertainty on the measurements was  $\pm 11\%$ . Thermal conductivity  $\kappa$  and thermal diffusivity  $a$  are related by the formula  $\kappa = aC_p\delta$  where  $C_p$  is the specific heat and  $\delta$  is the density measured by the Archimedean principle. Specific heat measurements were performed by the continuous scanning method under an argon atmosphere using a DSC 403 F3 apparatus (Netzsch). In the present case, the temperature dependence of  $\delta$  was neglected. The dimensionless thermoelectric figure of merit  $ZT$  was calculated from the relationship  $ZT = \alpha^2 T / \rho \lambda$  with an experimental uncertainty estimated to be  $\pm 17\%$ .

## 3. Results and discussion

### 3.1 Thermal properties of parent glasses: SPS experimental conditions for glass-ceramics elaboration

The glassy domain in the Cu-As-Te system obtained by melt-quenching is shown in Figure 1.<sup>29</sup>

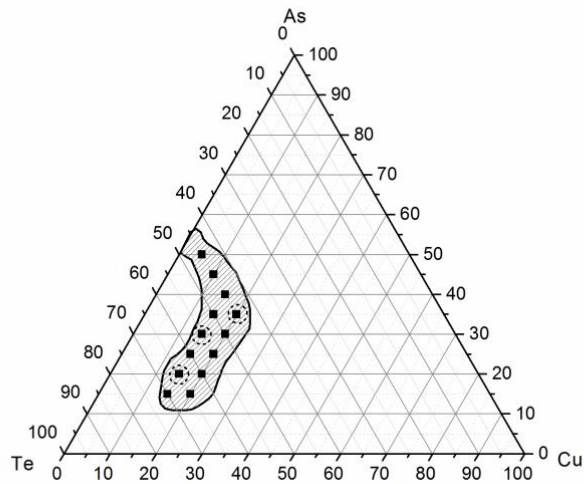


**Figure 1.** Vitreous domain and compositions of interest in the Cu-As-Te ternary system. The dashed circles correspond to the glass-ceramic compositions investigated in the present work.

In this system, three compositions (marked by dotted circles in Figure 1)  $\text{Cu}_{20}\text{As}_{35}\text{Te}_{45}$ ,  $\text{Cu}_{15}\text{As}_{30}\text{Te}_{55}$  and  $\text{Cu}_{15}\text{As}_{20}\text{Te}_{65}$  were chosen to elaborate glass-ceramics. The DSC thermograms of the three glassy compositions recorded with a heating rate of  $10 \text{ K}\cdot\text{min}^{-1}$  are shown in Figure 2. The glass transition temperature  $T_g$  and the glass stability, evaluated by the Dietzel criterion  $\Delta T = T_x - T_g$  where  $T_x$  is the temperature of the onset of the first crystallization peak, are 385 K ( $\Delta T = 38 \text{ K}$ ), 405 K ( $\Delta T = 34 \text{ K}$ ) and 433 K ( $\Delta T = 67 \text{ K}$ ) for  $\text{Cu}_{15}\text{As}_{20}\text{Te}_{65}$ ,  $\text{Cu}_{15}\text{As}_{30}\text{Te}_{55}$  and  $\text{Cu}_{20}\text{As}_{35}\text{Te}_{45}$ , respectively.

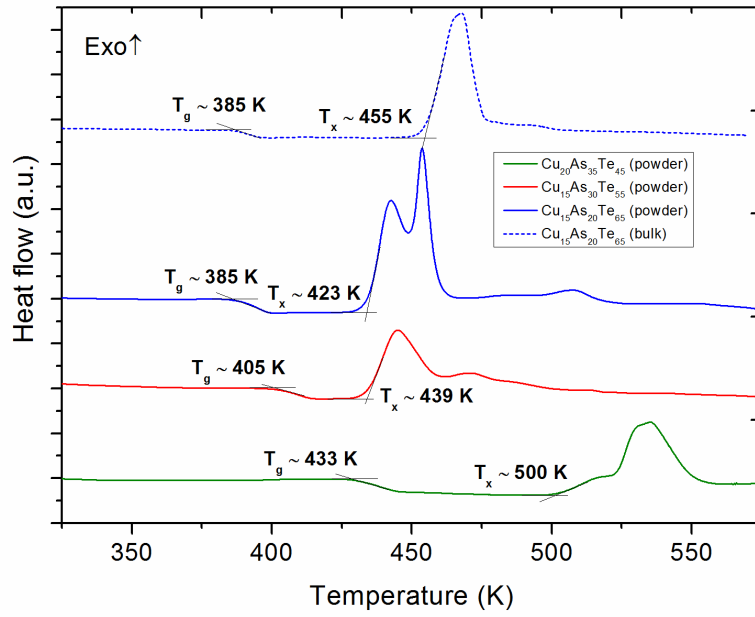


**Figure 2.** DSC curves of the glass compositions  $\text{Cu}_{15}\text{As}_{30}\text{Te}_{55}$  (powder),  $\text{Cu}_{15}\text{As}_{20}\text{Te}_{65}$  (bulk and powder),  $\text{Cu}_{20}\text{As}_{35}\text{Te}_{45}$  (powder).

A decrease in  $T_g$  when increasing the Te content is observed, consistent with a weaker structural rigidity. For all compositions, the Dietzel criterion is low, indicating that these glasses are rather unstable towards crystallization. The increase in the specific surface of the  $\text{Cu}_{15}\text{As}_{20}\text{Te}_{65}$  sample from bulk to powder causes a shift of the crystallization peaks towards lower temperatures (from  $T_x = 455$  K for bulk sample to  $T_x = 423$  K for powder sample). Such a trend is a clear signature of preferential surface crystallization.<sup>30</sup> The sintering of amorphous powders by SPS through viscous flow mechanisms is thus well adapted to obtain glass-ceramics with a significant volume fraction of crystalline phases.<sup>31</sup>

Based on the crystallization behavior determined by DSC data, we carried out a series of SPS experiments on the three compositions. The temperature and dwell time were the adjustable parameters while the pressure was maintained constant at 50 MPa. Our aim was to obtain either a glassy bulk material or a glass-ceramic with a controlled crystalline fraction. As a rough

estimation, the relative part of amorphous and crystalline domains was determined from EDXS-SEM images using an image-analysis software.

In order to be able to compare the transport properties in the three types of composite materials, glass-ceramics with similar crystalline fraction were elaborated for the three compositions. A crystalline fraction of 30% in volume was chosen to ensure that the electrical percolation threshold is reached.<sup>32</sup>

The SPS conditions to obtain glass-ceramics with a crystalline fraction of ~ 30 % in volume were found to be:

- 488 K, 5 minutes dwell time, 50 MPa for the  $\text{Cu}_{20}\text{As}_{35}\text{Te}_{45}$  composition ;
- 413 K, 20 minutes dwell time, 50 MPa for the  $\text{Cu}_{15}\text{As}_{30}\text{Te}_{55}$  composition ;
- 413 K, 5 minutes dwell time, 50 MPa for the  $\text{Cu}_{15}\text{As}_{20}\text{Te}_{65}$  composition.

Bulk glasses were obtained by consolidating amorphous powders by SPS through a viscous flow mechanism using temperatures and pressures similar to those used for glass-ceramics of similar compositions but with no dwell time applied.

### 3.2 Characterization of glass-ceramics

The amorphous nature of the samples after synthesis by melt-quenching was verified by PXRD measurements (Figure 3). The nature and chemical compositions of the phases crystallizing in the glassy matrix after the SPS treatment were determined by PXRD measurements combined with EDX (Figure 3). EPMA analysis revealed that the  $\text{Cu}_{15}\text{As}_{20}\text{Te}_{65}$  based glass-ceramic contains crystals with the  $\text{As}_{25}\text{Te}_{75}$  composition (see Supplementary Information, Figure S1). The well-defined peaks that show up in the  $\text{Cu}_{20}\text{As}_{35}\text{Te}_{45}$ ,  $\text{Cu}_{15}\text{As}_{30}\text{Te}_{55}$  and  $\text{Cu}_{15}\text{As}_{20}\text{Te}_{65}$  glassy matrices after SPS treatment correspond to the signature of  $\alpha\text{-As}_2\text{Te}_3$ ,  $\beta\text{-As}_2\text{Te}_3$  and  $\text{AsTe}_3$  phases, respectively.

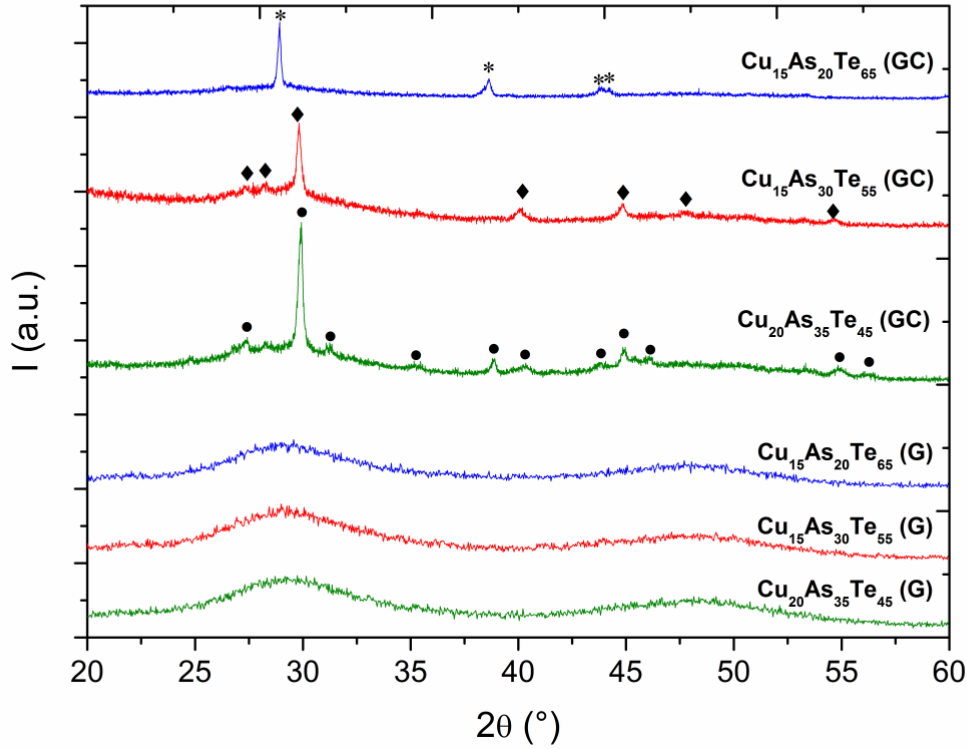


**Figure 3.** PXRD patterns of the  $\text{Cu}_{20}\text{As}_{35}\text{Te}_{45}$ ,  $\text{Cu}_{15}\text{As}_{30}\text{Te}_{55}$  and  $\text{Cu}_{15}\text{As}_{20}\text{Te}_{65}$  glasses (G) and their corresponding glass-ceramics (GC) prepared by Spark Plasma Sintering (SPS) with the respectively sintering conditions: 488 K, 50 MPa, 5 min. dwell time ( $\text{Cu}_{20}\text{As}_{35}\text{Te}_{45}$ ), 413 K, 50 MPa, 20 min. dwell time ( $\text{Cu}_{15}\text{As}_{30}\text{Te}_{55}$ ) and 413 K, 50 MPa, 5 min. dwell time ( $\text{Cu}_{15}\text{As}_{20}\text{Te}_{65}$ ). The symbols correspond to the crystalline phases: \*  $\text{AsTe}_3$ , ♦  $\beta\text{-As}_2\text{Te}_3$  and ●  $\alpha\text{-As}_2\text{Te}_3$ .

While  $\alpha\text{-As}_2\text{Te}_3$ , precipitated within the  $\text{Cu}_{20}\text{As}_{35}\text{Te}_{45}$  glassy matrix, is a stable phase in ambient conditions, the  $\beta\text{-As}_2\text{Te}_3$  polymorph is metastable and could be so far only synthesized under high-pressure or by rapid quenching.<sup>33-37</sup> The fact that the metastable high-pressure  $\beta\text{-As}_2\text{Te}_3$  phase is favored in the  $\text{Cu}_{15}\text{As}_{30}\text{Te}_{55}$  glass may be due either to the applied pressure during the SPS process or to the local stress-induced pressure due to the abrupt change in density. The stabilization of  $\beta\text{-As}_2\text{Te}_3$  in the glassy matrix has already proven to be an effective way to improve the thermoelectric performances of the glass thanks to the induced large decrease in

electrical resistivity combined with only a moderate increase in thermal conductivity.<sup>15</sup> Most interesting is the fact that an unreported and metastable phase,  $\text{AsTe}_3$  precipitates in the  $\text{Cu}_{15}\text{As}_{20}\text{Te}_{65}$  glass matrix upon crystallization. Such finding led us to investigate the direct synthesis of the  $\text{AsTe}_3$  phase, never reported earlier. All attempts failed except that described in section 2.1, that is, the full and congruent crystallization of the parent  $\text{AsTe}_3$  glass, which itself can only be obtained by the twin-roller quenching technique. An approximate crystal structure based on the neutron thermodiffraction data is reported in the present article. A full resolution of the crystal structure is currently in progress and will be reported in a forthcoming paper.<sup>38</sup>

Figure 4 shows backscattered electron mode-SEM images of the three glass-ceramics evidencing different microstructures. While the  $\alpha\text{-As}_2\text{Te}_3$  and  $\beta\text{-As}_2\text{Te}_3$  crystalline phases exhibit needle-like shape (Figures 4a and 4c),  $\text{AsTe}_3$  crystals form an assemblage of plate-like shape structure (Figure 4e). As previously shown by thermal analysis of both bulk samples and powders, surface crystallization plays a major role upon heating Cu-As-Te glasses. In the present samples, crystals are found to be disseminated within the whole volume of the glass-ceramics prepared by SPS from amorphous powders. It is noteworthy that the crystals form an infinite network of connected paths through the glassy matrix (Figures 4b, 4d and 4f). A clear chemical contrast is observed at the particle boundaries, which is a characteristic of surface devitrification phenomenon leading to the so-called “coast-and-island” microstructure. Such phenomenon is confirmed by high-resolution Raman scattering maps, which unambiguously demonstrate the localization of the crystals at the grain boundaries surrounded by amorphous grains.

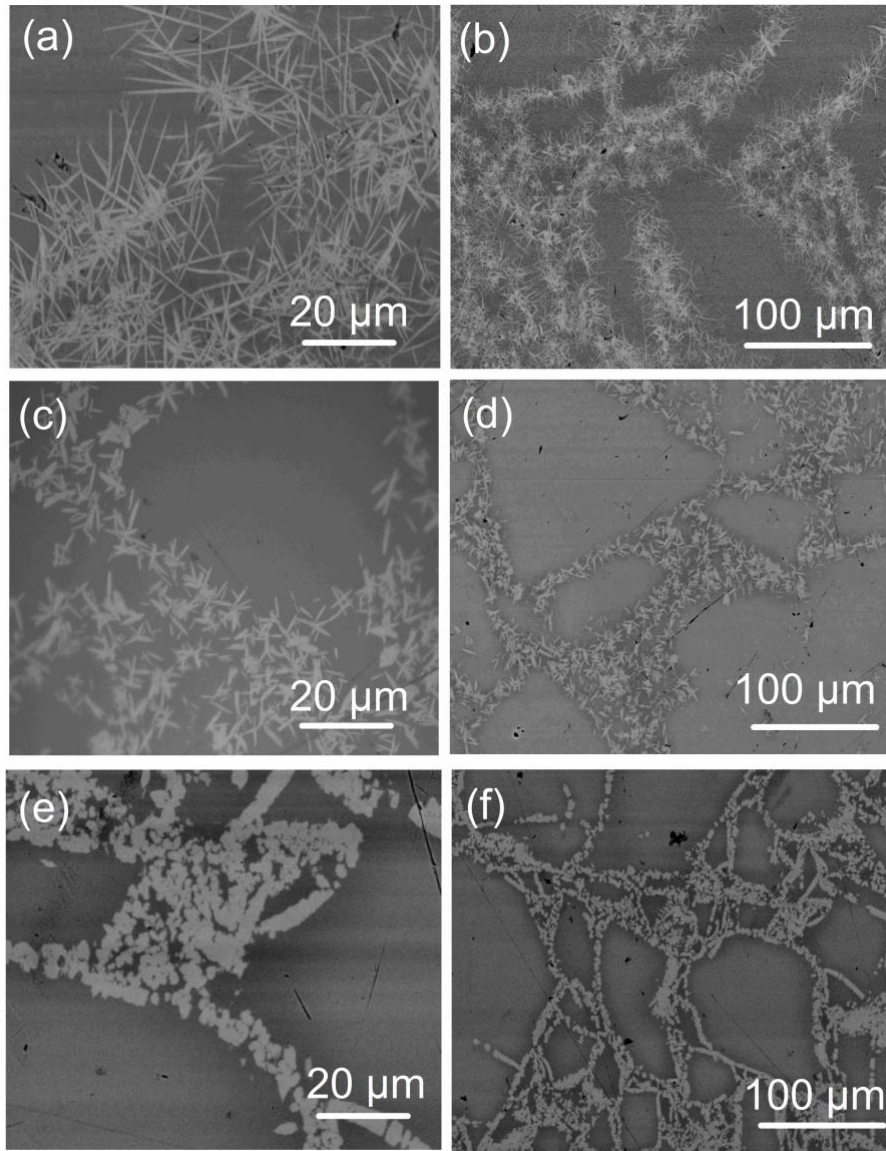


**Figure 4.** SEM images in backscattered electron mode of the microstructure of the different glass-ceramics  $\text{Cu}_{20}\text{As}_{35}\text{Te}_{45}$  at high (a) and low (b) magnifications,  $\text{Cu}_{15}\text{As}_{30}\text{Te}_{55}$  at high (c) and low (d) magnifications, and  $\text{Cu}_{15}\text{As}_{20}\text{Te}_{65}$  at high (e) and low (f) magnifications. These images show the crystallization of the  $\alpha\text{-As}_2\text{Te}_3$ ,  $\beta\text{-As}_2\text{Te}_3$  and  $\text{AsTe}_3$  compounds, respectively.

### 3.3 Neutron thermodiffraction

Neutron thermodiffraction experiments were carried out in order to get insights into the crystallization process occurring in the glassy matrices upon heating, *e.g.* the first phase that precipitates and its evolution with increasing temperature.

Figures 5a, 5b and 5c show the 2D thermodiffractograms collected between 460 and 488 K for  $\text{Cu}_{20}\text{As}_{35}\text{Te}_{45}$ ,  $\text{Cu}_{15}\text{As}_{30}\text{Te}_{55}$  and  $\text{Cu}_{15}\text{As}_{20}\text{Te}_{65}$ , respectively. The thermodiffractograms reveal that the crystallization process is sensitive to the starting composition. The  $\text{Cu}_{20}\text{As}_{35}\text{Te}_{45}$  and  $\text{Cu}_{15}\text{As}_{30}\text{Te}_{55}$  samples fully crystallize within a narrow temperature range after the appearance of the first crystallites ( $< 20$  K and  $< 5$  K, respectively). In contrast, a complex crystallization process with successive appearance of different phases occurs in the case of the  $\text{Cu}_{15}\text{As}_{20}\text{Te}_{65}$  composition. The temperature of first crystallization ( $T_x$ ) is lower when the Te content in the sample is larger. For the  $\text{Cu}_{15}\text{As}_{30}\text{Te}_{55}$  and  $\text{Cu}_{15}\text{As}_{20}\text{Te}_{65}$  glasses,  $T_x$  is estimated to  $\sim 394 - 400$  K while  $T_x$  is  $\sim 457$  K for the  $\text{Cu}_{20}\text{As}_{35}\text{Te}_{45}$  composition. These data are in good agreement with the DSC data where  $T_x \sim 423 - 439$  K for the  $\text{Cu}_{15}\text{As}_{30}\text{Te}_{55}$  and  $\text{Cu}_{15}\text{As}_{20}\text{Te}_{65}$  glasses and 500 K for the  $\text{Cu}_{20}\text{As}_{35}\text{Te}_{45}$  composition. The temperature difference between the two experiments can be explained by the different heating rates *i.e.*  $10 \text{ K}\cdot\text{min}^{-1}$  for DSC measurements and  $0.1 \text{ K}\cdot\text{min}^{-1}$  for neutron thermodiffraction. Increasing the heating rate shifts the thermal effects towards higher temperatures, a signature of a thermally activated process.

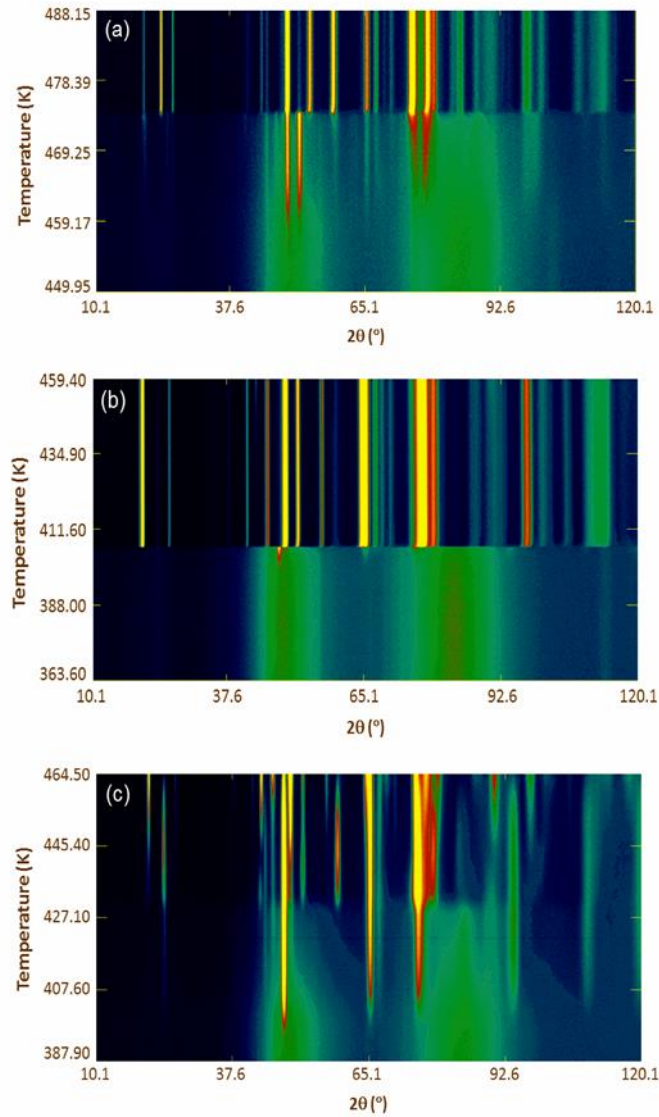


**Figure 5.** 2D plots of the neutron powder thermodiffraction data (nominal wavelength  $\lambda = 2.52$  Å) collected between  $10^\circ$  and  $120^\circ$  as a function of temperature for the (a)  $\text{Cu}_{20}\text{As}_{35}\text{Te}_{45}$ , (b)  $\text{Cu}_{15}\text{As}_{30}\text{Te}_{55}$  and (c)  $\text{Cu}_{15}\text{As}_{20}\text{Te}_{65}$  samples.

For  $\text{Cu}_{20}\text{As}_{35}\text{Te}_{45}$ , the first reflections at  $\sim 457$  K correspond to the stable  $\alpha\text{-As}_2\text{Te}_3$  phase (Figure 5a). Indeed, the four main peaks of this phase appear at  $2\theta = 49.3^\circ, 51.9^\circ, 75.3^\circ$  and  $77.3^\circ$  (Figures 6a and 6b). The crystallization of the sample is complete at 477K. Rietveld analysis of the diffractogram collected at this temperature reveals that the main phase present

in the compound is the monoclinic  $\alpha$ -As<sub>2</sub>Te<sub>3</sub> phase (57%) with Cu<sub>1.4</sub>Te (31%), As (9%) and AsTe (3%) as secondary phases (see Supplementary Information, Figure S2).

The sample Cu<sub>15</sub>As<sub>30</sub>Te<sub>55</sub> remains amorphous up to 405 K (Figure 5b). Beyond this limit, three peaks appear at 48.1°, 65.5° and 75.5° (Figures 6c and 6d) which correspond to the three main reflections of the metastable  $\beta$ -As<sub>2</sub>Te<sub>3</sub> phase. A further increase of ~ 2 K leads to the phase transition  $\beta \rightarrow \alpha$  and finally to the full crystallization of the sample. The Rietveld refinement of the diffractogram collected at 409K reveals that the phases present in the crystallized compound are the monoclinic  $\alpha$ -As<sub>2</sub>Te<sub>3</sub> phase (55%), CuTe (32%) and Te (13%) (see Supplementary Information, Figure S3). For both Cu<sub>20</sub>As<sub>35</sub>Te<sub>45</sub> and Cu<sub>15</sub>As<sub>30</sub>Te<sub>55</sub>, no evident change is observed beyond ~ 477 K and ~ 409 K, respectively.

The crystallization process for the glass Cu<sub>15</sub>As<sub>20</sub>Te<sub>65</sub> is more complex and involves several steps (Figure 5c). At about 394 K, a first crystalline phase corresponding to AsTe<sub>3</sub> appears, the existence of which has never been reported in the binary As – Te phase diagram. The three main peaks at  $2\theta = 48.0^\circ$ ,  $65.4^\circ$  and  $75.1^\circ$  have relative intensities of 100%, 35% and 34%, respectively (Figure 6e). The peak intensity first increases when the temperature increases up to about 445 K, then decreases with further increasing temperature, up to the end of the thermal treatment at ~ 465 K (see Fig. 5c). The AsTe<sub>3</sub> phase is the unique crystalline phase observed between 394K and 430K. As seen in Figures 5c and 6e, an intermediate phase appears at ~ 430 K. Its diffraction peaks correspond to the signature of Cu<sub>1.4</sub>Te (see Fig. 6f). The intermediate phase starts disappearing (as shown by the decrease in the diffraction peak intensity) at about 460K when a new series of crystallization peaks, signature of one or several new crystalline phases appear (see Figure 5c). The Rietveld refinement of the neutron pattern collected at 433K is shown in Fig. 7. Phase identification was easier at this temperature due to the well-established intensity of the secondary crystalline phases:  $\alpha$ -As<sub>2</sub>Te<sub>3</sub>, Cu<sub>1.4</sub>Te and AsTe.<sup>39,40,41</sup> The AsTe<sub>3</sub> pattern could be approximated by a modification of the  $\beta$ -As<sub>2</sub>Te<sub>3</sub>

structure<sup>39</sup>, for which the main changes are the expansion of the hexagonal lattice parameters to the values  $a = 4.134 \text{ \AA}$  and  $c = 30.728 \text{ \AA}$  as well as a random replacement of 37.5% of the As atoms in their  $6c$  site by Te atoms, to fulfill the 1:3 stoichiometry requirement. Because of the use of this approximant, weak lines remained unindexed and the reliability factors kept moderately large values ( $R_p = 16.9 \%$ ,  $R_{WP} = 21 \%$ , and  $\chi^2 = 12.2$ ). This Rietveld analysis thus strongly suggests that the crystalline phase  $\text{AsTe}_3$  is the main component at this temperature ( $\sim 67\%$ ,  $a = 4.134 \text{ \AA}$  and  $c = 30.728 \text{ \AA}$ ), before  $\alpha\text{-As}_2\text{Te}_3$  ( $\sim 14\%$ ,  $a = 14.126 \text{ \AA}$ ,  $b = 4.027 \text{ \AA}$ ,  $c = 10.041 \text{ \AA}$ ,  $\beta = 96.66^\circ$ ),  $\text{Cu}_{1.4}\text{Te}$  ( $\sim 16\%$ ,  $a = 3.981 \text{ \AA}$ ,  $b = 4.033 \text{ \AA}$ ,  $c = 6.119 \text{ \AA}$ ) and  $\text{AsTe}$  ( $\sim 3\%$ ,  $a = 5.767 \text{ \AA}$ ).

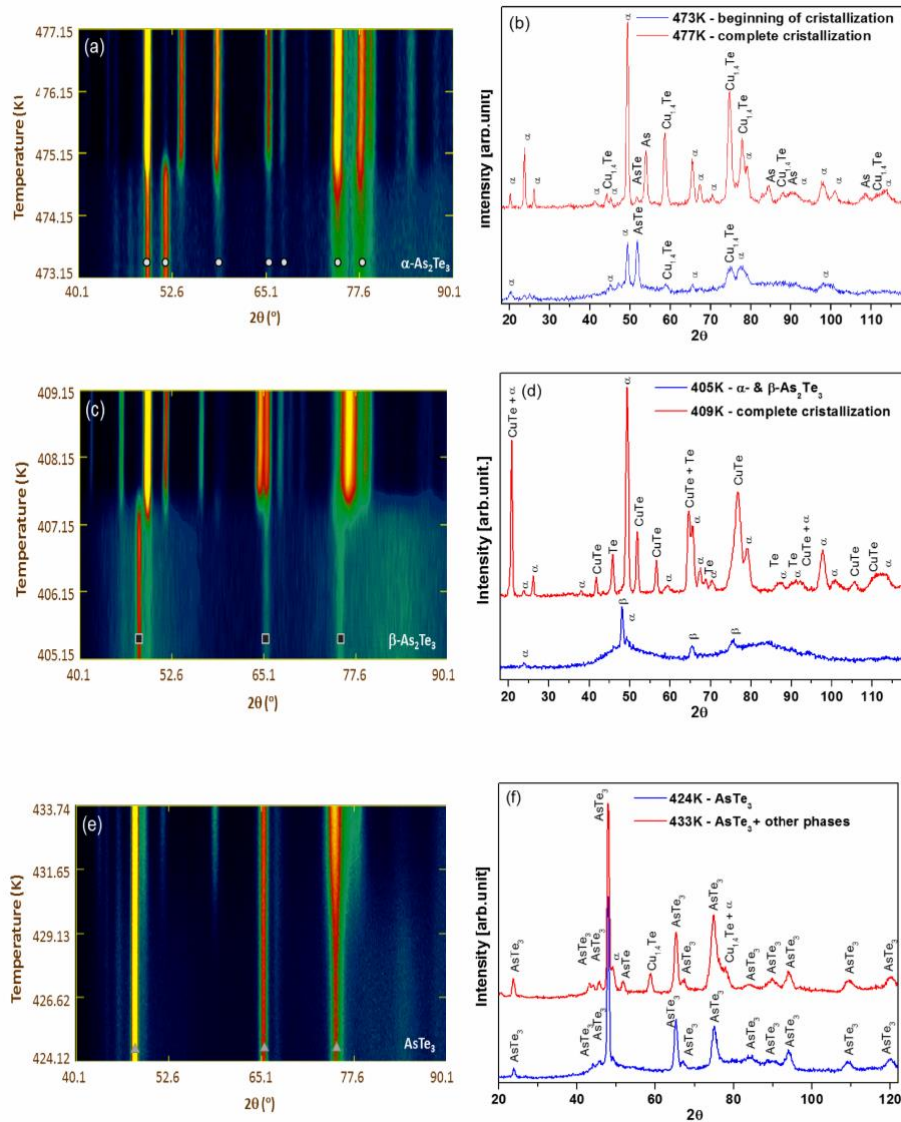


**Figure 6.** Magnification of the 2D maps of the neutron diffraction data of the (a)  $\text{Cu}_{20}\text{As}_{35}\text{Te}_{45}$ , (c)  $\text{Cu}_{15}\text{As}_{30}\text{Te}_{55}$  and (e)  $\text{Cu}_{15}\text{As}_{20}\text{Te}_{65}$  samples. The main reflections of the  $\alpha\text{-As}_2\text{Te}_3$ ,  $\beta\text{-As}_2\text{Te}_3$  and  $\text{AsTe}_3$  compounds are marked by their names. Neutron powder diffraction pattern highlighting the structural transition that sets in between 473 and 477 K for  $\text{Cu}_{20}\text{As}_{35}\text{Te}_{45}$  (b), 405 and 409 K for  $\text{Cu}_{15}\text{As}_{30}\text{Te}_{55}$  (d) and 424 and 433 K for  $\text{Cu}_{15}\text{As}_{20}\text{Te}_{65}$  (f).

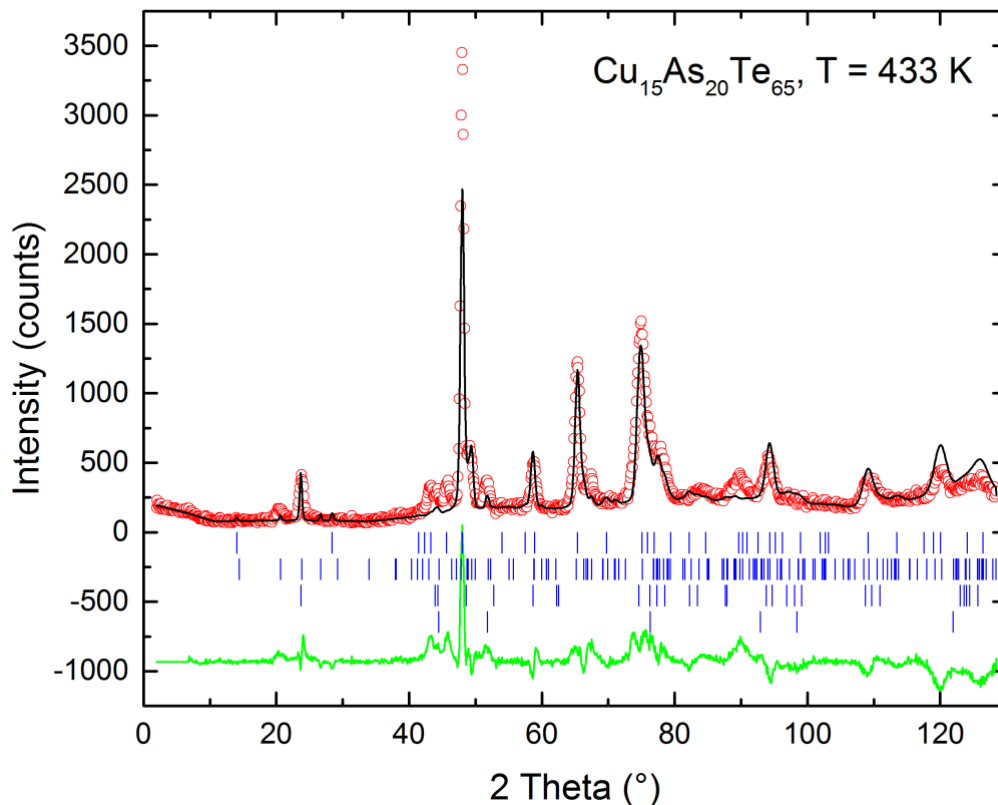


**Figure 7.** Rietveld refined neutron powder diffraction pattern recorded at 432K in  $\text{Cu}_{15}\text{As}_{20}\text{Te}_{65}$ . The red circles and the black line are the experimental and calculated pattern respectively. The green bottom line is the difference between experiment and calculations. The blue vertical ticks correspond to the Bragg position of the diffraction lines. The reliability factors for this refinement are  $R_p = 16.9\%$ ,  $R_{wp} = 21\%$ , and  $\chi^2 = 12.2$ .

The thermodiffraction data shows that the three first-phases to crystallize in the three glasses are the ones that were stabilized in the corresponding glass-ceramics, that is,  $\alpha\text{-As}_2\text{Te}_3$ ,

$\beta$ -As<sub>2</sub>Te<sub>3</sub> and AsTe<sub>3</sub> in the Cu<sub>20</sub>As<sub>35</sub>Te<sub>45</sub>, Cu<sub>15</sub>As<sub>30</sub>Te<sub>55</sub> and Cu<sub>15</sub>As<sub>20</sub>Te<sub>65</sub> glass compositions, respectively. Therefore, SPS appears as the process of choice to stabilize a crystalline phase in a glass-ceramics. It is particularly remarkable for  $\beta$ -As<sub>2</sub>Te<sub>3</sub> in the sample Cu<sub>15</sub>As<sub>30</sub>Te<sub>55</sub> owing to its very narrow domain of existence (~2 K). The applied pressure during the SPS process and/or internal stresses probably play an important role in the stabilization of this phase.

### **3.4 Comparative study of the three types of materials: glasses, glass-ceramics and pure crystalline phases**

#### 3.4.1 Raman experiments and lattice dynamics calculations

Figure 8 illustrates the reduced Raman spectra of both the crystals and the residual glassy matrix for the three different glass-ceramics. The broadening of the Raman peaks of the residual glassy matrix with respect to the embedded crystals evidences a higher degree of disorder in the glassy part. The three spectra collected on glasses are rather similar, each spectrum exhibiting three main bands in the frequency range 70-300 cm<sup>-1</sup> with approximate wavenumber positions at 150 cm<sup>-1</sup>, 190 cm<sup>-1</sup> and 220 cm<sup>-1</sup> attributed to Te-Te, As-Te and As-As stretching modes, respectively.<sup>42</sup> The main difference in the three Raman spectra lies in the change in intensity of these three bands. The Raman spectra of the crystals in the glass-ceramics exhibit three distinct shapes (Figure 8d). The detailed attributions of the bands will be discussed in detail below.

First, we recorded 2D Raman maps on each glass-ceramic (Figures 8a, 8b, 8c). The maps have been reconstructed by multivariate data analysis method (Direct Classical Least Squares component analysis, DCLS).

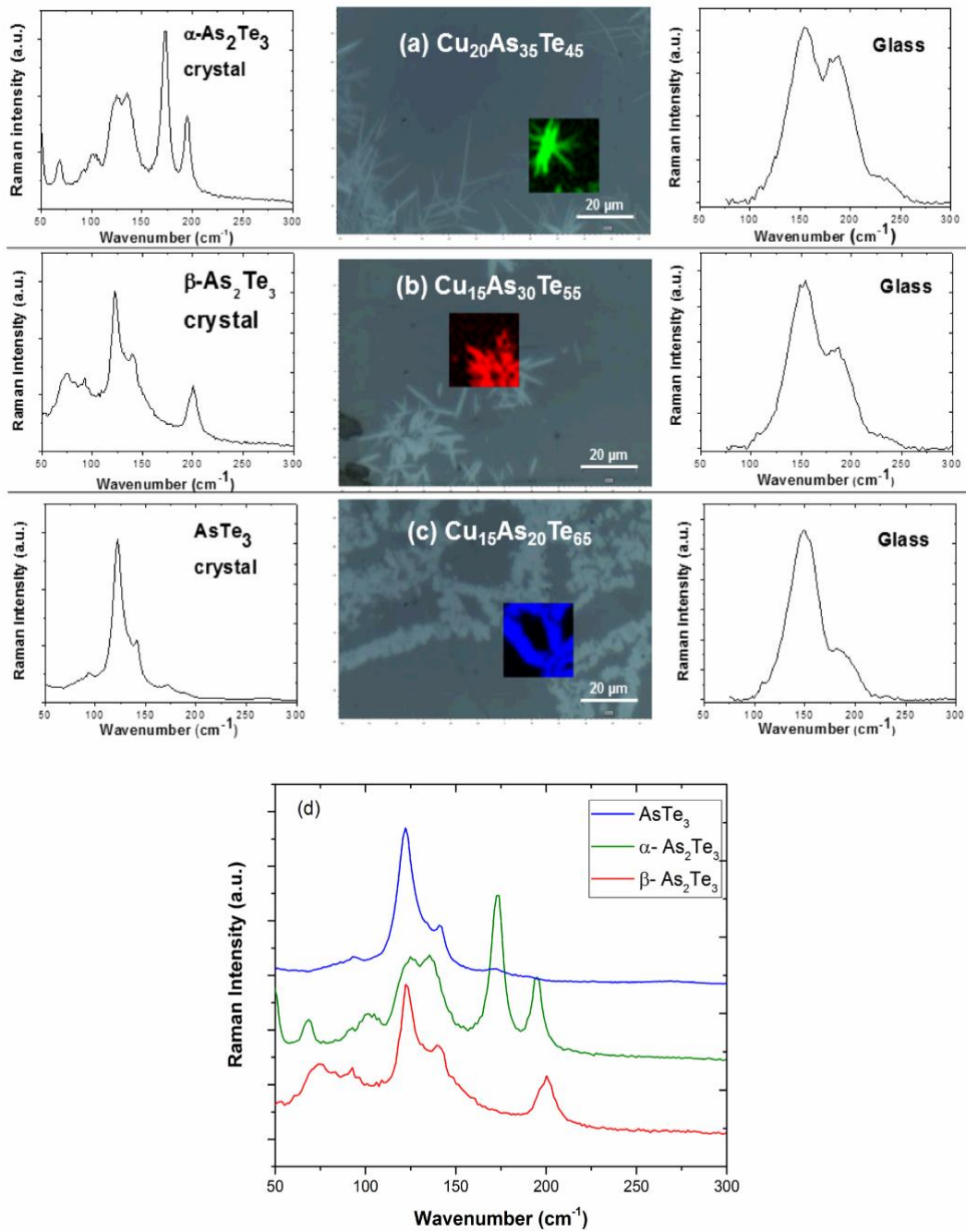


**Figure 8.** Raman scattering maps of the (a) Cu<sub>20</sub>As<sub>35</sub>Te<sub>45</sub> (b) Cu<sub>15</sub>As<sub>30</sub>Te<sub>55</sub> and (c) Cu<sub>15</sub>As<sub>20</sub>Te<sub>65</sub> related glass-ceramics. Left and right: Raman spectra correspond to the crystallized phase and glassy matrix, respectively (d) Raman spectra of the  $\alpha$ -As<sub>2</sub>Te<sub>3</sub>,  $\beta$ -As<sub>2</sub>Te<sub>3</sub> and AsTe<sub>3</sub> pure crystalline compounds.

We chose this method because reference spectra were available in both glassy matrix and crystalline part. The DCLS algorithm approximates the spectrum at each point in the map by

summing together scaled copies of each reference spectrum. The scaling factors are chosen to get the best possible fit to the original map spectrum and then used to create a map showing the distribution (correlation values) of reference spectrum (color contrasts). In the three samples, we obtained no lack of fit by using only two reference spectra, which is a signature of the crystallization of pure phases. Herein, we present only the maps reconstructed on the crystalline part (the black color is then linked to the glassy matrix). The maps clearly evidenced the crystallization of only one kind of phase in each glassy matrix:  $\alpha$ -As<sub>2</sub>Te<sub>3</sub> (green color) in Cu<sub>20</sub>As<sub>35</sub>Te<sub>45</sub>,  $\beta$ -As<sub>2</sub>Te<sub>3</sub> (red color) in Cu<sub>15</sub>As<sub>30</sub>Te<sub>55</sub>, AsTe<sub>3</sub> (blue color) in Cu<sub>15</sub>As<sub>20</sub>Te<sub>65</sub>.

Figures 9a and 9b show the Raman spectra of  $\alpha$ -As<sub>2</sub>Te<sub>3</sub> and  $\beta$ -As<sub>2</sub>Te<sub>3</sub> bulk materials under ambient conditions together with the theoretically predicted frequencies (marked by vertical ticks). In order to interpret the Raman spectra of the  $\alpha$ - and  $\beta$ -As<sub>2</sub>Te<sub>3</sub> compounds, lattice dynamics calculations have been performed using DFT.

From structure relaxation calculations with both PBE and PBE-D2 exchange-correlation functionals, we found that the calculated crystal lattice parameters are in better agreement with the experimental ones when van der Waals interaction is taken into account as with the PBE-D2 exchange-correlation functional.<sup>39,43</sup> This is especially evident concerning the rhombohedral angle  $\alpha_R$  for  $\beta$ -As<sub>2</sub>Te<sub>3</sub> and the lattice parameter  $a$  for monoclinic  $\alpha$ -As<sub>2</sub>Te<sub>3</sub> (see Tables 1 and 2). As these compounds are layered compounds, this is related to the nature of chemical bonding between the layers which are of van der Waals type and to the much larger van der Waals interspace between the layers in  $\beta$ -As<sub>2</sub>Te<sub>3</sub> than in Sb<sub>2</sub>Te<sub>3</sub> or Bi<sub>2</sub>Te<sub>3</sub>.<sup>39</sup>

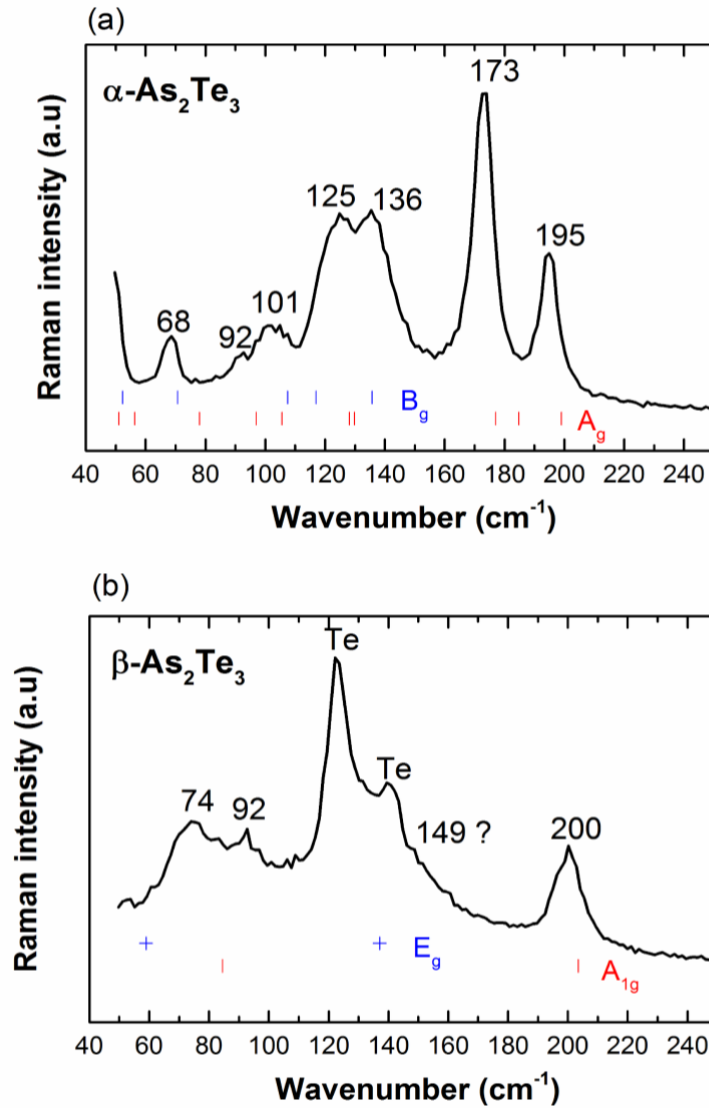


**Figure 9.** (a) Raman spectrum of the monoclinic  $\alpha$ -As<sub>2</sub>Te<sub>3</sub> phase together with the position of the Raman-active modes of A<sub>g</sub> symmetry (red ticks) and B<sub>g</sub> symmetry (blue ticks) calculated with DFPT, (b) Raman spectrum of the rhombohedral  $\beta$ -As<sub>2</sub>Te<sub>3</sub> phase together with the position of the Raman-active modes of A<sub>1g</sub> symmetry (red ticks) and E<sub>g</sub> symmetry (blue crosses) calculated with DFPT.

**Table 1.** Crystal parameters (in Å) of the  $\beta$ -As<sub>2</sub>Te<sub>3</sub> rhombohedral phase calculated by DFT with PBE and PBE-D2 exchange-correlation functionals compared to experiment results from Morin *et al.*<sup>39</sup>

<b>Crystal parameters</b>	<b>DFT (PBE-D2)</b>	<b>DFT (PBE)</b>	<b>Exper. (Morin)</b>
<b>a<sub>R</sub></b>	10.192	10.480	10.106
<b>α<sub>R</sub></b>	22.849	22.510	23.099
<b>z<sub>As</sub></b>	0.3947	0.3940	0.3977
<b>z<sub>Te2</sub></b>	0.2181	0.2205	0.2155

**Table 2.** Lattice parameters (in Å) of the  $\alpha$ -As<sub>2</sub>Te<sub>3</sub> monoclinic phase calculated by DFT with PBE and PBE-D2 exchange-correlation functionals compared to calculations with PBE exchange-correlation functional including spin-orbit and with experiment results from Cuenca-Gotor *et al.* and Morin *et al.*<sup>39,43</sup>

<b>Crystal parameters</b>	<b>DFT (PBE-D2)</b>	<b>DFT (PBE)</b>	<b>Exper. (Morin)</b>	<b>Exper. (Cuenca-Gotor)</b>	<b>DFT (PBE+SO) (Cuenca-Gotor)</b>
<b>a</b>	14.543	14.955	14.337	14.344	14.799
<b>b</b>	4.022	4.070	4.015	4.016	4.074
<b>c</b>	9.824	10.092	9.887	9.889	10.066
<b>β</b>	94.250	95.731	95.060	95.053	95.818

Of note, a better agreement with experiments was obtained for  $\alpha$ -As<sub>2</sub>Te<sub>3</sub> using the D2-PBE exchange-correlation functional without spin-orbit. These results thus contrast with the calculations performed by Cuenca-Gotor *et al.* who used PBE exchange-correlation functional including spin-orbit interaction.<sup>43</sup> This discrepancy suggests that the van der Waals interactions affect more significantly these calculations than the spin-orbit coupling does in these layered compounds. In good agreement with the experimental findings, we find that the monoclinic phase is more stable than the rhombohedral phase at 0 K by about -0.58 kJ/mole.at and -0.8 kJ/mole.at for the PBE-D2 and the PBE exchange-correlation functionals, respectively. The last value compares well with that calculated by Morin *et al.* (-0.96 kJ/mole.at) using similar PBE exchange-correlation functional.<sup>39</sup>

Hereafter, because the PBE-D2 exchange-correlation functional better describes the structure of both As<sub>2</sub>Te<sub>3</sub> phases, we will consider only the lattice dynamics calculations performed with this functional.

According to group theory, the decompositions of the lattice vibration modes in irreducible representation are the following:

- $\Gamma = 10 A_g \oplus 5 B_g \oplus 5 A_u \oplus 10 B_u$  (including the acoustic modes of  $A_u \oplus 2 B_u$  symmetry) for  $\alpha$ -As<sub>2</sub>Te<sub>3</sub>;
- $\Gamma = 2 A_{1g} \oplus 2 E_g \oplus 3 A_{2u} \oplus 3 E_u$  (including the acoustic modes of  $A_{2u} \oplus E_u$  symmetry) for  $\beta$ -As<sub>2</sub>Te<sub>3</sub>.

For  $\alpha$ -As<sub>2</sub>Te<sub>3</sub>, 15 Raman-active modes of  $A_g$  and  $B_g$  symmetry and 12 Raman-active modes of  $A_u$  and  $B_u$  symmetry exist while for  $\beta$ -As<sub>2</sub>Te<sub>3</sub>, only 4 Raman-active modes of  $A_{1g}$  and  $E_g$  symmetry and 4 Raman-active modes of  $A_{2u}$  and  $E_u$  symmetry are present.

As seen in Figure 9, the agreement of our calculations with experiments is quite reasonable for the full phonon spectra of both As<sub>2</sub>Te<sub>3</sub> crystalline phases. More specifically, above 150 cm<sup>-1</sup>, we found a slightly larger Raman shift for the higher energy Raman active

mode at about  $200\text{ cm}^{-1}$  in the case of the  $\beta\text{-As}_2\text{Te}_3$  phase compared to the  $\alpha\text{-As}_2\text{Te}_3$  phase, as experimentally observed (Figure 9). These modes correspond to As-Te stretching-like modes with  $A_g$  and  $A_{1g}$  symmetry for the  $\alpha$ - and  $\beta\text{-As}_2\text{Te}_3$  phases, respectively. In the case of  $\beta\text{-As}_2\text{Te}_3$ , the Te1 atoms located in the center of the layers remain motionless. The twofold degenerated  $E_g$  modes and the  $A_{1g}$  modes correspond to motions within the layers (intra-layer vibrations) and along the  $c$  direction *i.e.* perpendicular to the layers (inter-layer vibrations), respectively. The two highest-energy  $A_{1g}$  and  $E_g$  modes involve large motions of the lighter As atoms while this trend is reversed for the two lowest energy  $A_{1g}$  and  $E_g$  modes. In the case of  $\alpha\text{-As}_2\text{Te}_3$ , the nature of the modes are more complex and the motions of atoms are along the monoclinic  $b$  direction and within the  $ac$  plane for the  $B_g$  modes and  $A_g$  modes, respectively.

Below  $150\text{ cm}^{-1}$ , the presence of modes at about  $122$  and  $140\text{ cm}^{-1}$  due to elemental tellurium in some of the spectra can make difficult the assignments of the modes.<sup>43,44</sup> This is especially true for the  $\beta\text{-As}_2\text{Te}_3$  phase since our calculations show that one  $E_g$  mode is present slightly below  $140\text{ cm}^{-1}$ . One can tentatively assign the shoulder at about  $150\text{ cm}^{-1}$  to this mode but further experiments are necessary before drawing a definitive conclusion. Concerning the monoclinic phase, the agreement between the Raman spectra obtained in the present work and in the work of Cuenca-Gotor *et al.* is rather good, the main difference coming from different amounts of elemental tellurium in the samples.<sup>43</sup> However, our calculations are not in agreement with some of the phonon mode assignments made by Cuenca-Gotor *et al.* for the monoclinic phase using lattice dynamics calculations performed with PBE functional that describes the structure less accurately. For example, the mode at  $99\text{ cm}^{-1}$  should have  $A_g$  symmetry contrary to the assignment made by Cuenca-Gotor *et al.* Finally, in the case of  $\text{AsTe}_3$ , one can assign the modes at  $122$  and  $140\text{ cm}^{-1}$  to elemental Te and the mode at about  $170\text{ cm}^{-1}$  to  $\alpha\text{-As}_2\text{Te}_3$ .<sup>43,44</sup> The presence of these elements might be due to partial decomposition of metastable  $\text{AsTe}_3$  induced by laser heating during data collection. However, we assign the

rather broad peak at about  $93\text{ cm}^{-1}$  to  $\text{AsTe}_3$  because none of the above phases has intense Raman mode in this spectral range.

### 3.4.2 Transport properties

Figures 10a-e show the temperature dependence of the electrical resistivity  $\rho$ , thermopower  $\alpha$ , power factor  $\alpha^2/\rho$ , total thermal conductivity  $\lambda$  and dimensionless thermoelectric figure of merit  $ZT$  of the  $\text{Cu}_{20}\text{As}_{35}\text{Te}_{45}$ ,  $\text{Cu}_{15}\text{As}_{30}\text{Te}_{55}$  and  $\text{Cu}_{15}\text{As}_{20}\text{Te}_{65}$  glasses and glass-ceramics. Similar information for the pure  $\alpha\text{-As}_2\text{Te}_3$ ,  $\beta\text{-As}_2\text{Te}_3$  and  $\text{AsTe}_3$  crystalline phases is shown in Figure 11. Because of their layered crystalline structure, the measurements on the polymorphic  $\text{As}_2\text{Te}_3$  compounds were carried out both parallel and perpendicular to the pressing direction of the dense pellets. Data derived from measurements at 375 K for all samples (glasses, glass-ceramics and crystalline phases) are listed in Table 3 for comparison.

For all compositions, crystallization of glasses leads to a drastic decrease in the electrical resistivity by at least two orders of magnitude. This phenomenon points to the presence of a percolation network achieved for each glass-ceramics, as suggested by the particle surface crystallization observed on SEM images. For  $\text{Cu}_{20}\text{As}_{35}\text{Te}_{45}$ , the measured  $\rho$  values are even lower than those obtained for the pure  $\alpha\text{-As}_2\text{Te}_3$  crystalline phase. In contrast to the  $\alpha\text{-As}_2\text{Te}_3$  and  $\text{AsTe}_3$  crystalline phases that behave as semiconductors, the electrical properties of both the  $\beta\text{-As}_2\text{Te}_3$  crystalline compound and glass-ceramics ( $\text{Cu}_{20}\text{As}_{35}\text{Te}_{45}$  and  $\text{Cu}_{15}\text{As}_{30}\text{Te}_{55}$ ) are characteristic of metallic systems with relatively low  $\rho$  and  $\alpha$  values. According to the effective medium theory, the transport properties of a composite are bound by the properties of each of the constitutive phase of the composite.<sup>32,45-47</sup> Thus, this theory rules out any significant effects of the phase distribution on the overall thermoelectric efficiency.

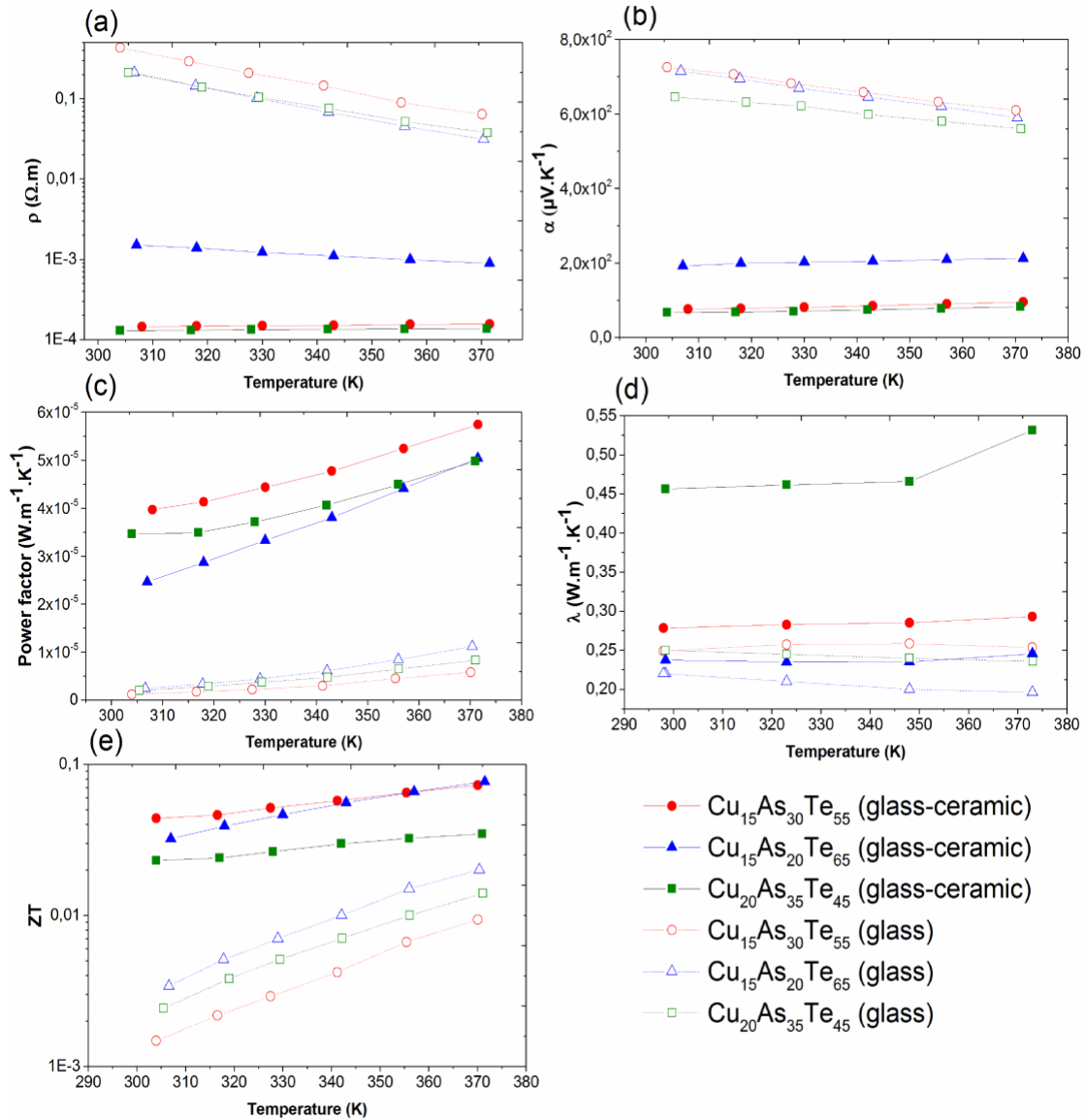


**Figure 10.** (a) Electrical resistivity  $\rho$ , (b) thermopower  $\alpha$ , (c) power factor, (d) total thermal conductivity  $\lambda$  and (e) figure of merit  $ZT$  as a function of temperature for the  $\text{Cu}_{20}\text{As}_{35}\text{Te}_{45}$ ,  $\text{Cu}_{15}\text{As}_{30}\text{Te}_{55}$  and  $\text{Cu}_{15}\text{As}_{20}\text{Te}_{65}$  parent glasses and glass-ceramics. All the measurements were performed parallel to the pressing direction.

The different behaviors observed between the crystalline and composite compounds may then be explained by different actual compositions of the phases crystallized from the glassy matrix and synthesized separately. As in  $\text{Bi}_2\text{Te}_3$ , small deviations from the ideal stoichiometry

in both  $\alpha$ -As<sub>2</sub>Te<sub>3</sub> and  $\beta$ -As<sub>2</sub>Te<sub>3</sub> are present and strongly affect the thermoelectric properties through variations in the carrier concentration.<sup>20,35,48</sup>

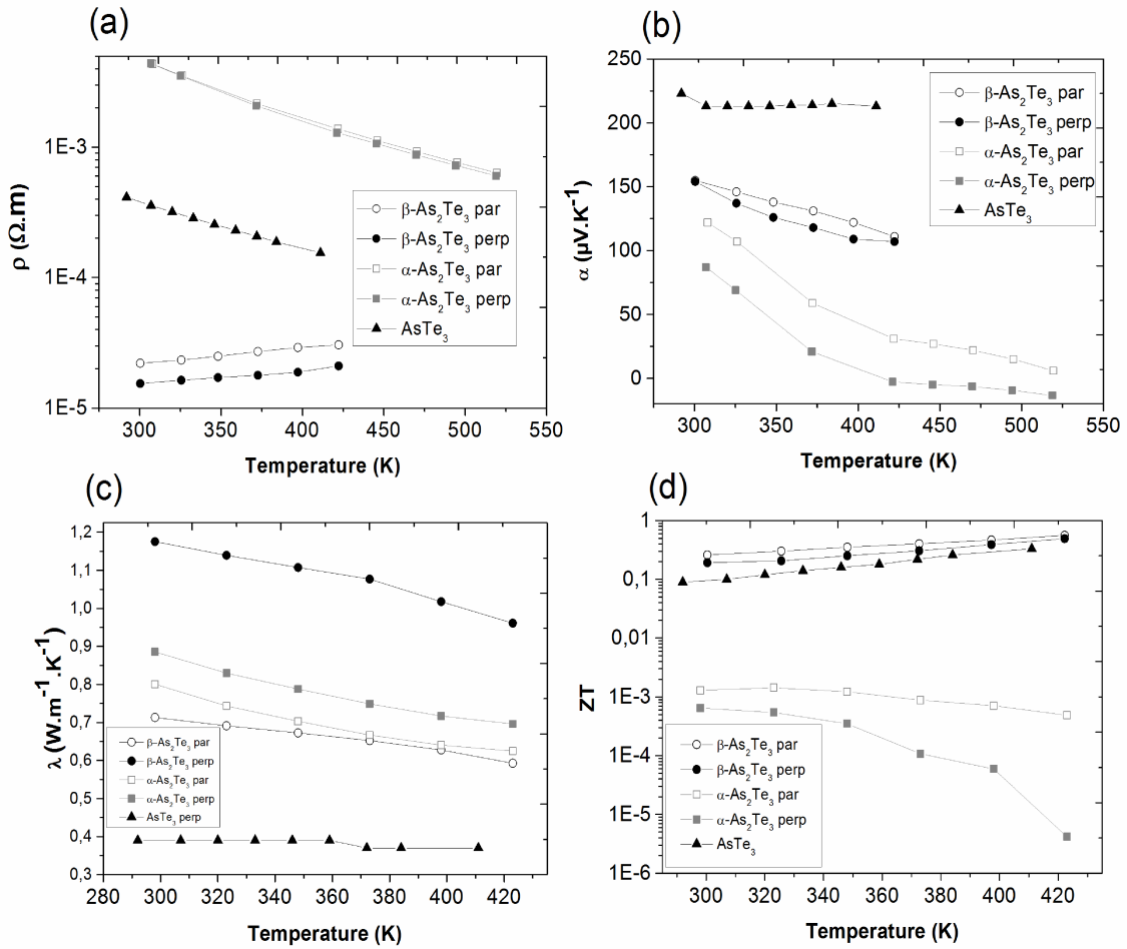


**Figure 11.** (a) Electrical resistivity  $\rho$ , (b) thermopower  $\alpha$ , (c) total thermal conductivity  $\lambda$  and (d) thermoelectric figure of merit  $ZT$  as a function of temperature for the  $\alpha$ -As<sub>2</sub>Te<sub>3</sub>,  $\beta$ -As<sub>2</sub>Te<sub>3</sub>, and AsTe<sub>3</sub> pure crystalline phases.

Perso, j'enlèverais cette figure. Les données ne sont pas tellement décrites dans le papier et pour AsTe<sub>3</sub>, si on montre ses propriétés, on ne pourra plus les mettre dans l'autre papier. Le tableau 3 me semble suffisant pour ne pas trop dévoiler ses propriétés.

**Table 3.** Density, crystalline fraction and thermoelectric properties of the  $\text{Cu}_{20}\text{As}_{35}\text{Te}_{45}$ ,  $\text{Cu}_{15}\text{As}_{30}\text{Te}_{55}$  and  $\text{Cu}_{15}\text{As}_{20}\text{Te}_{65}$  glass compositions, their corresponding glass-ceramics and the pure  $\alpha\text{-As}_2\text{Te}_3$ ,  $\beta\text{-As}_2\text{Te}_3$  and  $\text{AsTe}_3$  crystalline phases at 375 K. (Some thermoelectric properties were measured perpendicular  $\perp$  and parallel  $\parallel$  to the pressing direction).

Composition	Structure	Density ( $\text{g.cm}^{-3}$ )	$f_{\text{cryst}}$ (%)	$\rho$ ( $\Omega.\text{m}$ )	$\alpha$ ( $\mu\text{V.K}^{-1}$ )	Power Factor ( $\text{W.m}^{-1}.\text{K}^{-2}$ )	$\lambda$ ( $\text{W.m}^{-1}.\text{K}^{-1}$ )	ZT
$\text{Cu}_{20}\text{As}_{35}\text{Te}_{45}$	Glass	5.92	0	$3.5 \cdot 10^{-2}$	550	$8.6 \cdot 10^{-6}$	0.24	$1.4 \cdot 10^{-2}$
	Glass-ceramic	6.14	30	$1.4 \cdot 10^{-4}$	82.6	$49.8 \cdot 10^{-6}$	0.53	$3.47 \cdot 10^{-2}$
$\alpha\text{-As}_2\text{Te}_3$	Crystal	6.23	100	$2.2 \cdot 10^{-3} \parallel$	59 $\parallel$	$1.6 \cdot 10^{-6} \parallel$	0.67 $\parallel$	$9.0 \cdot 10^{-4} \parallel$
				$2.1 \cdot 10^{-3} \perp$	21 $\perp$	$2.1 \cdot 10^{-7} \perp$	0.75 $\perp$	$1.1 \cdot 10^{-4} \perp$
$\text{Cu}_{15}\text{As}_{30}\text{Te}_{55}$	Glass	5.90	0	$5.5 \cdot 10^{-2}$	600	$7.1 \cdot 10^{-6}$	0.24	$1.0 \cdot 10^{-2}$
	Glass-ceramic	6.08	27	$1.6 \cdot 10^{-4}$	94.6	$57.2 \cdot 10^{-6}$	0.29	$7.3 \cdot 10^{-2}$
$\beta\text{-As}_2\text{Te}_3$	Crystal	6.28	100	$2.7 \cdot 10^{-5} \parallel$	131 $\parallel$	$6.4 \cdot 10^{-4} \parallel$	0.65 $\parallel$	0.37 $\parallel$
				$1.8 \cdot 10^{-5} \perp$	118 $\perp$	$7.7 \cdot 10^{-4} \perp$	1.08 $\perp$	0.27 $\perp$
$\text{Cu}_{15}\text{As}_{20}\text{Te}_{65}$	Glass	6.01	0	$2.6 \cdot 10^{-2}$	580	$13.0 \cdot 10^{-6}$	0.20	$2.2 \cdot 10^{-2}$
	Glass-ceramic	6.12	29	$2.12 \cdot 10^{-4}$	212	$50.4 \cdot 10^{-6}$	0.24	$7.8 \cdot 10^{-2}$
$\text{AsTe}_3$	Crystal	6.20	100	$2.1 \cdot 10^{-4} \parallel$	214 $\parallel$	$2.2 \cdot 10^{-4} \parallel$	0.34 $\parallel$	0.24 $\parallel$

Partial crystallization of the glasses systematically results in a decrease in the  $\alpha$  values, which can be attributed to a higher thermopower of the precipitated crystalline phases. In addition, effective medium theory applied to thermopower demonstrated that above the percolation threshold of the most conductive phase (which is likely achieved in the present samples), the  $\alpha$  values of two-phase materials tend rapidly to that of the most conducting phase.<sup>32,49</sup> Assuming that this applies in the present case, a rough estimate of the thermopower of the crystallites for each glass-ceramic can be inferred. The  $\text{Cu}_{20}\text{As}_{35}\text{Te}_{45}$  and  $\text{Cu}_{15}\text{As}_{30}\text{Te}_{55}$  glass-ceramics that stabilize  $\alpha\text{-As}_2\text{Te}_3$  and  $\beta\text{-As}_2\text{Te}_3$  crystalline phases respectively, exhibit  $\alpha$

values of 70 and 80  $\mu\text{V K}^{-1}$  at 300 K. These results are in fair agreement with the average values of 100 and 150  $\mu\text{V K}^{-1}$  measured on pure polycrystalline samples. For the  $\text{Cu}_{15}\text{As}_{20}\text{Te}_{65}$  glass-ceramic that stabilizes  $\text{AsTe}_3$ , the  $\alpha$  value of 200  $\mu\text{V K}^{-1}$  at 300 K compares well with that measured on the polycrystalline sample. Considering the synthesis method of polycrystalline  $\text{AsTe}_3$  from congruent crystallization of amorphous  $\text{AsTe}_3$ , it is no surprise that roughly the same properties are obtained. The discrepancy observed for the binaries  $\text{As}_2\text{Te}_3$  further underlines the difference in nature between the  $\alpha$ - $\text{As}_2\text{Te}_3$  and  $\beta$ - $\text{As}_2\text{Te}_3$  crystallites found in the glass-ceramics and those directly synthesized. The power factor of each glass-ceramic is increased by only one order of magnitude compared to that of the corresponding glass. Indeed, the overall significant decrease in electrical resistivity is counterbalanced by the decrease in  $\alpha$  values. The maximum power factors achieved for the glass-ceramics fall in the range 50 – 100  $\mu\text{W m}^{-1} \text{K}^{-2}$ , that is, still one order of magnitude lower than in efficient thermoelectric materials.

The evolution of the thermal conductivity  $\lambda$  with the nature of the crystalline phase is also intriguing (Figure 10d). Regardless of the nature of the crystallized phase, the  $\lambda$  values remain very low (0.5  $\text{W m}^{-1} \text{K}^{-1}$ ). For both  $\text{Cu}_{15}\text{As}_{30}\text{Te}_{55}$  and  $\text{Cu}_{15}\text{As}_{25}\text{Te}_{65}$ , the  $\lambda$  values are within the range of those typically measured in chalcogenide glasses (0.3  $\text{W m}^{-1} \text{K}^{-1}$ ). Due to the high electrical resistivity values that yield a negligible electronic contribution, the measured  $\lambda$  values solely reflect the lattice contribution. The slight increase in  $\lambda$  in  $\text{Cu}_{15}\text{As}_{30}\text{Te}_{55}$  and  $\text{Cu}_{15}\text{As}_{25}\text{Te}_{65}$  is therefore remarkable and emphasizes the role of the “coast-and-island” microstructure with the percolated conducting phase and the complex dendritic local microstructure of the  $\text{As}_2\text{Te}_3$  phases both of which likely acting as efficient phonon scatterers.

Finally, despite an enhancement of the  $ZT$  values in all glass-ceramics compared to their respective parent glasses, the electrical resistivity values remain too high to yield interesting thermoelectric properties. Nevertheless, an almost sevenfold increase in  $ZT$  is achieved in  $\text{Cu}_{15}\text{As}_{30}\text{Te}_{55}$  glass-ceramic with a value of 0.07 at 375 K. This value is similar to that observed

for this particular composition in our prior study.<sup>15</sup> A similar maximum  $ZT$  value of 0.08 is reached at 375 K in the  $\text{Cu}_{15}\text{As}_{25}\text{Te}_{65}$  glass-ceramic.

### 3 Conclusion

The influence of partial crystallization of Cu-As-Te glasses on their microstructural and physical properties was studied for three different  $\text{Cu}_{20}\text{As}_{30}\text{Te}_{45}$ ,  $\text{Cu}_{15}\text{As}_{30}\text{Te}_{55}$  and  $\text{Cu}_{15}\text{As}_{25}\text{Te}_{65}$  compositions. The differences in the chemical composition along with the versatility of the SPS technique allow for fine tuning of the phases crystallizing in the glassy matrices. The results evidenced the possibility to crystallize  $\alpha\text{-As}_2\text{Te}_3$ ,  $\beta\text{-As}_2\text{Te}_3$  or the as-yet unknown binary  $\text{AsTe}_3$  phases among which the latter two are metastable under ambient conditions. The thermodiffraction data confirms that these crystalline phases are the first to precipitate in the corresponding glasses, that is,  $\alpha\text{-As}_2\text{Te}_3$ ,  $\beta\text{-As}_2\text{Te}_3$  and  $\text{AsTe}_3$  in  $\text{Cu}_{20}\text{As}_{35}\text{Te}_{45}$ ,  $\text{Cu}_{15}\text{As}_{30}\text{Te}_{55}$  and  $\text{Cu}_{15}\text{As}_{20}\text{Te}_{65}$  glass compositions, respectively. A complementary study by Raman spectroscopy coupled with DFT calculations taking into account van der Waals interactions provides an accurate description of the lattice dynamics in both  $\text{As}_2\text{Te}_3$  phases.

Glass-ceramics with nearly comparable crystalline fractions (30% in volume) were successfully prepared, which enabled an objective comparison of the influence of the nature of the crystalline phase on the glass-ceramic physical properties. Raman spectroscopy mapping coupled to SEM unambiguously show the localization of the crystallites within the glassy matrix revealing a “coast-and-island” microstructure. This microstructure, ideal to ensure an electrical percolation of the highly-conducting ordered phase, results in a drastic decrease in electrical resistivity accompanied by a very moderate increase in the thermal conductivity. This study may pave the way to the fabrication of either known or yet-to-be discovered novel compounds by glass recrystallization.

## **Acknowledgements**

The authors would like to thank financial support from the French National Agency (ANR) in the frame of its program “PROGELEC” (Verre Thermo-Générateur “VTG”).

## References

- [1] X. Zhang, Y. Guimond, Y. Bellec, *J. Non-Cryst. Solids*, 2003, **326**, 519.
- [2] B. Bureau, X.H. Zhang, F. Smektala, J.-L. Adam, J. Troles, H.-l. Ma, C. Boussard-Pledel, J. Lucas, P. Lucas, D. Le Coq, *J. Non-Cryst. Solids*, 2004, **345**, 276.
- [3] P. Dos Santos, M. De Araujo, A. Gouveia-Neto, J.M. Neto, A. Sombra, *Appl. Phys. Lett.*, 1998, **73**, 578.
- [4] W. Zhang, V.L. Deringer, R. Dronskowski, R. Mazzarello, E. Ma, M. Wuttig, *MRS Bulletin*, 2015, **40**, 856.
- [5] M. Wuttig, *Phys. Status Solidi B*, 2012, **249**, 1843.
- [6] J. Sanghera, I. Aggarwal, *J. Non-Cryst. Solids*, 1999, **256**, 6.
- [7] T. Hakari, M. Nagao, A. Hayashi, M. Tatsumisago, *J. Power Sources*, 2015, **293**, 721.
- [8] Y. Seino, T. Ota, K. Takada, A. Hayashi, M. Tatsumisago, *Energy Environ. Sci.*, 2014, **7**, 627.
- [9] S. Kondo, K. Takada, Y. Yamamura, *Solid State Ionics*, 1992, **53**, 1183.
- [10] A.P. Gonçalves, E.B. Lopes, G. Delaizir, J.B. Vaney, B. Lenoir, A. Piarristeguy, A. Pradel, J. Monnier, P. Ochin, C. Godart, *J. Sol. Stat. Chem.*, 2012, **193**, 26.
- [11] A.P. Gonçalves, G. Delaizir, E.B. Lopes, L.M. Ferreira, O. Rouleau, C. Godart, *J. Electron. Mater.*, 2011, **40**, 1015.
- [12] A. Pereira Gonçalves, E. Branco Lopes, O. Rouleau, C. Godart, *J. Mater. Chem.*, 2010, **20**, 1516.
- [13] P. Lucas, C. Conseil, Z. Yang, Q. Hao, S. Cui, C. Boussard-Pledel, B. Bureau, F. Gascoin, C. Caillaud, O. Gulbiten, T. Guizouarn, P. Baruah, Q. Li, J. Lucas, *J. Mater. Chem. A*, 2013, **1**, 8917.
- [14] J.B. Vaney, A. Piarristeguy, A. Pradel, E. Alleno, B. Lenoir, C. Candolfi, A. Dauscher, A.P. Gonçalves, E.B. Lopes, G. Delaizir, J. Monnier, M. Ribes, C. Godart, *J. Sol. Stat. Chem.*, 2013, **203**, 212.
- [15] J.B. Vaney, A. Piarristeguy, A. Pradel, E. Alleno, B. Lenoir, C. Candolfi, A. Dauscher, A.P. Gonçalves, E.B. Lopes, G. Delaizir, J. Monnier, M. Ribes, C. Godart, *J. Mater. Chem. A*, 2013, **1**, 8190.
- [16] B. Poudel, Q. Hao, Y. Ma, Y. Lan, A. Minnich, B. Yu, X. Yan, D. Wang, A. Muto, D. Vashaee, X. Chen, J. Liu, M. S. Dresselhaus, G. Chen, Z. Ren, *Science*, 2008, **320**, 634.

- [17] C. M. Jaworski, V. Kulbachinskii, J. P. Heremans, *Phys. Rev. B: Condens. Matter Mater. Phys.* 2009, **80**, 233201.
- [18] W. Xie, J. He, H. Jung Kang, X. Tang, S. Zhu, M. Laver, S. Wang, J. R. D. Copley, C. M. Brown, Q. Zhang, T. M. Tritt, *Nano Lett*, 2010, **10**, 3283.
- [19] S. I. Kim, K. H. Lee, H. A. Mun, H. S. Kim, S. W. Hwang, J. W. Roh, D. J. Yang, W. H. Shin, X. S. Li, Y. H. Lee, G. J. Snyder, S. W. Kim, *Science* 2015, **348**, 109.
- [20] J. B. Vaney, J. Carreaud, G. Delaizir, E. Alleno, A. Piarristeguy, J. Monnier, C. Morin, A. Pradel, A. P. Gonçalves, C. Candolfi, A. Dauscher, B. Lenoir, *Adv. Elec. Mater.*, 2015, **1**, 1400008.
- [21] A. Piarristeguy, E. Barthélémy, M. Krbal, J. Frayret, C. Vigreux, A. Pradel, *J. Non-Cryst. Sol.*, 2009, **355**, 2088.
- [22] J. Rodriguez-Carvajal, *Physica B*, 1993, **192**, 55-69.
- [23] V. F. Sears, *Neutron news*, 1992, **3**, 26.
- [24] G. Kresse and J. Furthmüller, *Phys. Rev. B*, 1996, **54**, 11169.
- [25] G. Kresse, D. Joubert, *Phys. Rev. B*, 1999, **59**, 1758.
- [26] J.-P. Perdew, K. Burke, M. Erzenhof, *Phys. Rev. Lett.*, 1996, **77**, 3865.
- [27] S. Grimme, *J. Comp. Chem.*, 2006, **27**, 1787.
- [28] M. Gajdoš, K. Hummer, G. Kresse, J. Furthmüller, and F. Bechstedt, *Phys. Rev. B*, 2006, **73**, 045112.
- [29] Z. U. Borisova, *Glassy Semiconductors* (1985) Plenum Press.
- [30] From glass to crystal: Nucleation, growth and phase separation: from research to applications, Daniel R. Neuville, Laurent Cornier, Daniel Caurant et Lionel Montagne, EDP Sciences - Collection : Science des matériaux (2017).
- [31] A. Bertrand, J. Carreaud, G. Delaizir, J.-R. Duclere, M. Colas, J. Cornette, M. Vandenhende, V. Couderc, P. Thomas, *J. Amer. Ceram. Soc.*, 2014, **97**, 163.
- [32] J.-B. Vaney, J. Carreaud, G. Delaizir, C. Morin, J. Monnier, E. Alleno, A. Piarristeguy, A. Pradel, A. P. Gonçalves, E. B. Lopes, C. Candolfi, A. Dauscher, B. Lenoir, *J. Mater. Chem. C*, 2015, **3**, 11090.
- [33] T. C. Harman, B. Paris, S. E. Miller, H. L. Goering, *J. Phys. Chem. Solids*, 1957, **2**, 181.
- [34] G. J. Carron, *Acta Cryst.*, 1963, **16**, 338.
- [35] J. B. Vaney, J. Carreaud, G. Delaizir, C. Morin, J. Monnier, E. Alleno, A. Piarristeguy, A. Pradel, A. P. Gonçalves, E. B. Lopes, C. Candolfi, A. Dauscher, B. Lenoir, *J. Electron. Mater.* 2016, **45**, 1447.
- [36] H. W. Shu, S. Jaulmes, J. Flahaut, *J. Solid State Chem.*, 1988, **74**, 277.

- [37] K. Pal , U. V. Waghmare, *Appl. Phys. Lett.*, 2014, **105**, 062105.
- [38] J. B. Vaney, C. Morin, J. Carreaud, C. Candolfi, A. Piarristeguy, G. Delaizir, M. Bigot, J. Monnier, E. Alleno, M. Ribes, A. Pradel, E.B. Lopes, A.P. Goncalves, V. Nassif, G. J. Cuello, B. Lenoir, Thermoelectric properties of new AsTe<sub>3</sub> crystalline compound, in preparation.
- [39] C. Morin, S. Corallini, J. Carreaud, J.-B. Vaney, G. Delaizir, J.-C. Crivello, E. Branco Lopes, A. Piarristeguy, J. Monnier, C. Candolfi, V. Nassif, G. J. Cuello, A. Pradel, A. Pereira Goncalves, B. Lenoir, E. Alleno, *Inorg. Chem.*, 2015, 54, 9936.
- [40] A. L. N. Stevels and G. A. Wiegers, *Rec. Trav. Chim. Pays-Bas*, 1971, **90**, 352-359.
- [41] R. K. Quinn, *Mater. Res. Bull.*, 1974, **9**, 803-813.
- [42] A. Tverjanovich, K. Rodionov, E. Bychkov, *J. Solid Stat. Chem.*, 2012, **190**, 271.
- [43] V. P. Cuenca-Gotor, J. A. Sans, J. Ibanez, C. Popescu, O. Gomis, R. Vilaplana, F; J. Manjon, A. Leonardo, E. Sagasta, A. Suarez-Alcubilla, I. G. Gurtubay, M. Mollar, A. Bergara, *J. Phys. Chem. C*, 2016, **120**, 19340.
- [44] A. S. Pine, M. S. Dresselhaus, *Phys. Rev. B*, 1971, **4**, 356.
- [45] V. Odelevskii, *Zh. Tekh. Fiz.*, 1951, **21**, 678.
- [46] R. Landauer, *J. Applied Phys.*, 1952, **23**, 779.
- [47] D. S. McLachlan, M. Blaszkiewicz, R.E. Newnham, *J. Am. Ceram. Soc.*, 1990, **73**, 2187.
- [48] J. B. Vaney, J. Carreaud, G. Delaizir, A. Piarristeguy, A. Pradel, E. Alleno, J. Monnier, E. B. Lopes, A. P. Goncalves, A. Dauscher, C. Candolfi B. Lenoir, *J. Mater. Chem. C*, 2016, **4**, 2329.
- [49] A. Snarskii, I. Bezudnov, *Journal of Thermoelectricity*, 2005, **3**, 7.

## Table captions

**Table 1.** Crystal parameters (in Å) of the  $\beta$ -As<sub>2</sub>Te<sub>3</sub> rhombohedral phase calculated by DFT with PBE and PBE-D2 exchange-correlation functionals compared to experiment results from Morin *et al.* [Morin].

**Table 2.** Lattice parameters (in Å) of the  $\alpha$ -As<sub>2</sub>Te<sub>3</sub> monoclinic phase calculated by DFT with PBE and PBE-D2 exchange-correlation functionals compared to calculations with PBE exchange-correlation functional including spin-orbit and with experiment results from Cuenca-Gotor *et al.* [Cuenca-Gotor] and Morin *et al.* [Morin].

**Table 3.** Density, crystalline fraction and thermoelectric properties of the Cu<sub>20</sub>As<sub>35</sub>Te<sub>45</sub>, Cu<sub>15</sub>As<sub>30</sub>Te<sub>55</sub> and Cu<sub>15</sub>As<sub>20</sub>Te<sub>65</sub> glass compositions, their corresponding glass-ceramics and the pure  $\alpha$ -As<sub>2</sub>Te<sub>3</sub>,  $\beta$ -As<sub>2</sub>Te<sub>3</sub> and AsTe<sub>3</sub> crystalline phases at 375 K. (Some thermoelectric properties were measured in the perpendicular  $\perp$  and parallel  $\parallel$  direction of the pressing direction).

## Figure captions

**Figure 1.** Vitreous domain and compositions of interest in the Cu-As-Te ternary system. The dashed circles correspond to the glass-ceramic compositions investigated in the present work.

**Figure 2.** DSC curves of the glass compositions  $\text{Cu}_{15}\text{As}_{30}\text{Te}_{55}$  (powder),  $\text{Cu}_{15}\text{As}_{20}\text{Te}_{65}$  (bulk and powder),  $\text{Cu}_{20}\text{As}_{35}\text{Te}_{45}$  (powder).

**Figure 3.** XRD patterns (nominal wavelength  $\lambda_{\text{Cu}} = 1.54 \text{ \AA}$ ) of the  $\text{Cu}_{20}\text{As}_{35}\text{Te}_{45}$ ,  $\text{Cu}_{15}\text{As}_{30}\text{Te}_{55}$  and  $\text{Cu}_{15}\text{As}_{20}\text{Te}_{65}$  glasses (G) and their corresponding glass-ceramics (GC) prepared by Spark Plasma Sintering (SPS) with the respectively sintering conditions: 488 K, 50 MPa, 5 min. dwell time ( $\text{Cu}_{20}\text{As}_{35}\text{Te}_{45}$ ), 413 K, 50 MPa, 20 min. dwell time ( $\text{Cu}_{15}\text{As}_{30}\text{Te}_{55}$ ) and 413 K, 50 MPa, 5 min. dwell time ( $\text{Cu}_{15}\text{As}_{20}\text{Te}_{65}$ ). The symbols correspond to the crystalline phases: \*  $\text{AsTe}_3$ ,  $\blacklozenge$   $\beta\text{-As}_2\text{Te}_3$  and  $\bullet$   $\alpha\text{-As}_2\text{Te}_3$ .

**Figure 4.** SEM images in backscattered electron mode of the microstructure of the different glass-ceramics  $\text{Cu}_{20}\text{As}_{35}\text{Te}_{45}$  at high (a) and low (b) magnifications,  $\text{Cu}_{15}\text{As}_{30}\text{Te}_{55}$  at high (c) and low (d) magnifications, and  $\text{Cu}_{15}\text{As}_{20}\text{Te}_{65}$  at high (e) and low (f) magnifications. These images show the crystallization of the  $\alpha\text{-As}_2\text{Te}_3$ ,  $\beta\text{-As}_2\text{Te}_3$  and  $\text{AsTe}_3$  compounds, respectively.

**Figure 5.** 2D plots of the neutron powder thermodiffraction data (nominal wavelength  $\lambda = 2.52 \text{ \AA}$ ) collected between  $10^\circ$  and  $120^\circ$  as a function of temperature for the (a)  $\text{Cu}_{20}\text{As}_{35}\text{Te}_{45}$ , (b)  $\text{Cu}_{15}\text{As}_{30}\text{Te}_{55}$  and (c)  $\text{Cu}_{15}\text{As}_{20}\text{Te}_{65}$  samples.

**Figure 6.** Magnification of the 2D maps of the neutron diffraction data of the (a)  $\text{Cu}_{20}\text{As}_{35}\text{Te}_{45}$ , (c)  $\text{Cu}_{15}\text{As}_{30}\text{Te}_{55}$  and (e)  $\text{Cu}_{15}\text{As}_{20}\text{Te}_{65}$  samples. The main reflections of the  $\alpha$ - $\text{As}_2\text{Te}_3$ ,  $\beta$ - $\text{As}_2\text{Te}_3$  and  $\text{AsTe}_3$  compounds are marked by the circle, square and triangle symbols, respectively. Neutron powder diffraction pattern highlighting the structural transition that sets in between 473 and 477 K for  $\text{Cu}_{20}\text{As}_{35}\text{Te}_{45}$  (b), 405 and 409 K for  $\text{Cu}_{15}\text{As}_{30}\text{Te}_{55}$  (d) and 424 and 433 K for  $\text{Cu}_{15}\text{As}_{20}\text{Te}_{65}$  (f).

**Figure 7.** Rietveld refined neutron powder diffraction pattern recorded at 432K in  $\text{Cu}_{15}\text{As}_{20}\text{Te}_{65}$ . The red circles and the black line are the experimental and calculated pattern respectively. The green bottom line is the difference between experiment and calculations. The blue vertical ticks correspond to the Bragg position of the diffraction lines. The reliability factors for this refinement are  $R_p = 16.9\%$ ,  $R_{wp} = 21\%$ , and  $\chi^2 = 12.2$ .

**Figure 8.** Raman scattering maps of the (a)  $\text{Cu}_{20}\text{As}_{35}\text{Te}_{45}$  (b)  $\text{Cu}_{15}\text{As}_{30}\text{Te}_{55}$  and (c)  $\text{Cu}_{15}\text{As}_{20}\text{Te}_{65}$  related glass-ceramics. Left and right: Raman spectra correspond to the crystallized phase and glassy matrix, respectively (d) Raman spectra of the  $\alpha$ - $\text{As}_2\text{Te}_3$ ,  $\beta$ - $\text{As}_2\text{Te}_3$  and  $\text{AsTe}_3$  pure crystalline compounds.

**Figure 9.** (a) Raman spectrum of the monoclinic  $\alpha$ - $\text{As}_2\text{Te}_3$  phase together with the position of the Raman-active modes of  $A_g$  symmetry (red ticks) and  $B_g$  symmetry (blue ticks) calculated with DFPT, (b) Raman spectrum of the rhombohedral  $\beta$ - $\text{As}_2\text{Te}_3$  phase together with the position of the Raman-active modes of  $A_{1g}$  symmetry (red ticks) and  $E_g$  symmetry (blue crosses) calculated with DFPT.

**Figure 10.** (a) Electrical resistivity  $\rho$ , (b) thermopower  $\alpha$ , (c) power factor, (d) total thermal conductivity  $\lambda$  and (e) figure of merit  $ZT$  as a function of temperature for the  $\text{Cu}_{20}\text{As}_{35}\text{Te}_{45}$ ,  $\text{Cu}_{15}\text{As}_{30}\text{Te}_{55}$  and  $\text{Cu}_{15}\text{As}_{20}\text{Te}_{65}$  parent glasses and glass-ceramics.

**Figure 11.** (a) Electrical resistivity  $\rho$ , (b) thermopower  $\alpha$ , (c) total thermal conductivity  $\lambda$  and (d) figure of merit  $ZT$  as a function of temperature for the  $\alpha$ - $\text{As}_2\text{Te}_3$ ,  $\beta$ - $\text{As}_2\text{Te}_3$ , and  $\text{AsTe}_3$  pure crystalline phases.